arXiv:astro-ph/9911320v1 17 Nov 1999

UMN-TH-1826/99
TPI-MINN-99-51
astro-ph/9911320
November 1999

TESTING SPALLATION PROCESSES WITH BERYLLIUM AND BORON

Brian D. Fields
Department of Astronomy
University of Illinois
Urbana, IL 61801, USA

Keith A. Olive
Theoretical Physics Institute
School of Physics and Astronomy
University of Minnesota
Minneapolis, MN 55455, USA

Elisabeth Vangioni-Flam
Institut d'Astrophysique, 98 bis Boulevard Arago
Paris 75014, France

Michel Cassé
Service d'Astrophysique, CEA, Orme des Merisiers
91191 Gif sur Yvette, France
and
Institut d'Astrophysique, 98 bis Boulevard Arago
Paris 75014, France

ABSTRACT

The nucleosynthesis of Be and B by spallation processes provides unique insight into the origin of cosmic rays. Namely, different spallation schemes predict sharply different trends for the growth of LiBeB abundances with respect to oxygen. "Primary" mechanisms predict BeB $\propto$ O, and are well motivated by the data if O/Fe is constant at low metallicity. In contrast, "secondary" mechanisms predict BeB $\propto O^2$ and are consistent with the data if O/Fe increases towards low metallicity as some recent data suggest. Clearly, any primary mechanism, if operative, will dominate early in the history of the Galaxy. In this paper, we fit the BeB data to a two-component scheme which includes both primary and secondary trends. In this way, the data can be used to probe the period in which primary mechanisms are effective. We

analyze the data using consistent stellar atmospheric parameters based on Balmer line data and the continuum infrared flux. Results depend sensitively on Pop II O abundances and, unfortunately, on the choice of stellar parameters. When using recent results which show O/Fe increasing toward lower metallicity, a two-component Be-O fits indicates that primary and secondary components contribute equally at $[O/H]_{eq} = -1.8$ for Balmer line data; and $[O/H]_{eq} = -1.4$ to -1.8 for IRFM. We apply these constraints to recent models for LiBeB origin. The Balmer line data does not show any evidence for primary production. On the other hand, the IRFM data does indicate a preference for a two-component model, such as a combination of standard GCR and metal-enriched particles accelerated in superbubbles. These conclusions rely on a detailed understanding of the abundance data including systematic effects which may alter the derived O-Fe and BeB-Fe relations.

1. Introduction

The light elements beryllium and boron (BeB) provide unique insight into the nature of non-thermal nucleosynthesis in our Galaxy. Due to their low binding energy, these nuclei are not produced significantly in the big bang (Thomas, Schramm, Olive, & Fields 1993, Delbourgo-Salvador & Vangioni-Flam 1993) or in stellar nuclear burning. Instead, BeB are made by spallation processes due to energetic nuclei and neutrinos. The nucleosynthesis origin of BeB is in principle encoded in their abundances in the most primitive, metal poor (Population II) stars. Indeed, the mere presence of Be in halo stars is perhaps the strongest evidence that accelerated particles were present in the early Galaxy.[1] Thus, in this paper we will focus on Pop II BeB trends, via a detailed analysis of the data and a comparison with recent models.

The production of BeB by Galactic cosmic ray (GCR) spallation of interstellar CNO nuclei was the standard model for BeB nucleosynthesis for almost two decades after first being proposed (Reeves, Fowler, & Hoyle 1970; Meneguzzi, Audouze, & Reeves 1971). However, this simple model was challenged by the observations of BeB abundances in Pop II stars, and particularly the BeB trends versus metallicity. Measurements showed that both Be and B vary roughly *linearly* with Fe, a so-called "primary" scaling. In contrast, standard GCR nucleosynthesis predicts that BeB should be "secondary" versus spallation targets CNO, giving Be $\propto$ O^2 (Vangioni-Flam, Cassé, Audouze, & Oberto 1990). If O and Fe are co-produced (i.e., if O/Fe is constant) then the data clearly contradicts the canonical theory, i.e. BeB production via standard GCR's.

BeB abundances in Pop II stars have thus provided the motivation for primary BeB nucleosynthesis, in which the production rate is independent of metallicity. These primary models invoke the extraction and acceleration of fresh products of nucleosynthesis (α's, CO) originating from Type II supernovae and Wolf-Rayet stars and fragmenting on interstellar H and He. They should be considered in addition to the standard GCR (secondary) process; any primary process would be expected to play a major role in the early Galaxy (halo phase), whereas the secondary one takes over in the galactic disk (Cassé *et al.* 1995, Vangioni-Flam *et al.* 1996) or earlier as we shall see. The transition between the two modes may vary depending on the adopted BeB data, as well as the [O/Fe] vs [Fe/H] correlation.

One such primary model has focused on superbubbles–regions of hot, rarefied, metal-rich gas swept out by the collective effects of massive star winds and supernova explosions. These regions have been proposed (Vangioni-Flam et al. 1998; Higdon *et al.* 1998; Ramaty & Lingenfelter 1999; Parizot 1998; Vangioni-Flam, Cassé & Audouze 1999) to accelerate freshly synthesized, metal-rich particles. The energy spectrum of these nuclei has been extensively studied by Bykov (1999,1995) and it is remarkably similar to the GCR injection spectrum. Finally, core collapse supernovae

[1]Pop II lithium abundances are dominated by the primordial ^{7}Li component, which must be subtracted to provide information about Galactic Li sources. Elemental Li is discussed in Ryan, Beers, Olive, Fields, & Norris (1999); the Li isotopes are analyzed in Vangioni-Flam *et al.* (1999) and Fields & Olive (1999b).

themselves have been proposed as a site of ^{11}B production (and some ^{7}Li) via spallation reactions between supernova neutrinos passing through the ^{12}C layer, the "ν-process" (Woosley *et al.* 1990).

Recently, another solution has been proposed to resolve discrepancy between the observed BeB abundances as a function of metallicity and the predicted secondary trend of GCR spallation. As noted above, standard GCR nucleosynthesis predicts Be $\propto$ O^2, while observations show Be $\sim$ Fe, roughly; these two trends are inconsistent if O/Fe is constant in Pop II. However, recent observations find O/Fe increasing at low metallicities (Israelian, García-López, & Rebolo 1998; Boesgaard *et al.* 1999a). In fact Boesgaard *et al.* (1999a) argue for a single slope of $\simeq -0.35$ for O/Fe vs. Fe *at all* metallicities. As shown by Fields & Olive (1999a), a combination of standard GCR nucleosynthesis, and ν-process production of ^{11}B is consistent with current data. One should note that while the trend in O/Fe is seen in the OH data and agrees with the O I triplet (Boesgaard *et al.* 1999a), they continue to disagree with the observations of O/H using the forbidden [O I] line (Fulbright & Kraft 1999).

It is clear that spallation processes, BeB abundances, and O-Fe evolution are closely linked. In this paper, we explore these connections via careful analysis of both data and theory. We use the most current BeB data, with abundances derived from consistent stellar atmosphere models. We consider stellar parameters based the Balmer-line data of Axer, Fuhrmann, & Gehren (1994) and the IRFM (Alonso *et al.* 1996b). We first fit the data to both iron and oxygen to determine the overall primary vs. secondary nature of the BeB abundances. These data are fit to a two-component, primary plus secondary, metallicity dependence. This fit quantifies both the strength of each component as well as the metallicity and hence epoch as which the secondary component becomes dominant.

We compare these phenomenological results to the predictions of current models for BeB nucleosynthesis and chemical evolution. We find that for the Balmer line data, any primary component could only have been dominant at oxygen abundances [O/H] < -1.8, which is at metallicities below the existing data. That is, for this data set, we find no evidence for primary BeB production. In contrast, for the IRFM data, we find that primary production dominates for [O/H] < -1.4 to -1.8 (depending on the exact data-see below). The higher value indicates indicating the need for a primary mechanism at low metallicities. If O/Fe is constant then the transition between primary and secondary production processes would occur at [Fe/H] ≈ -1. As such, our quantitative conclusions can not be definitive. The derivation of the oxygen abundance from the observed spectra is delicate, specifically at low metallicity. Moreover, non local thermodynamic equilibrium (NLTE) effects on Fe could affect substantially the BeB-Fe relationship. We also point out that since magnesium is not plagued by the same difficulties regarding the stellar yields of Fe, it would be worthwhile to examine the relationship of the BeB elements with Mg. New observations are eagerly awaited.

2. Data Sets

The BeB-OFe abundance trends encode the history of spallation in the Galaxy. Our ability to infer this history is completely determined by the accuracy of the abundance data studied. It is thus necessary to obtain high quality data. Just as importantly, the abundances must be combined in a systematic and consistent way.

The determination of abundances from raw stellar spectra requires stellar atmosphere models. The atmospheric models require key input parameters, notably the effective temperature $T_{\rm eff}$ and surface gravity g, and assumptions regarding, e.g., the applicability of local thermodynamic equilibrium (LTE). Unfortunately, there is no standard set of stellar parameters for the halo stars of interest. In practice, different groups derive abundances via different procedures, which give similar results but retain systematic differences. The systematic differences in the data can in fact obscure the BeB-OFe trends one seeks. Thus, to derive meaningful BeB fits, one must systematically and consistently present abundances derived under the same assumptions and parameters for stellar atmospheres.

Below, we will present results based for the available BeBOFe data based on two methods of analysis. We will refer to these as the Balmer line data and the IRFM data. The Balmer line data is taken from the work of Axer, Fuhrmann, & Gehren (1994) and Fuhrmann, Axer, & Gehren (1993). These authors have studied over 100 dwarf and subgiant stars to determine a consistent set of stellar parameters which includes the effective temperature, surface gravity and iron abundance. The effective temperatures are determined from the synthesis of the first four Balmer lines. This amounts to a spectroscopic rather than a photometric determination of the effective temperature. The remaining parameters were determined simultaneously from the analysis of a number of iron lines. The temperatures determined this way are typically 100–200 K higher than many of the photometric determinations in the literature. The [Fe/H] abundance determined by Axer, Fuhrmann, & Gehren (1994) are also typically higher than others sometimes by as much as 0.5 dex. It goes without saying that such differences can have an enormous effect in trying to establish a trend for BeB vs. Fe.

An alternative method to obtain effective temperatures is achieved by comparing the bolometric flux and the IR flux at a fixed wavelength. This method, knows as the IRFM, requires only the theoretical prediction of the continuum IR flux. There is a slight dependence on the assumed surface gravity and metallicity. A large compilation of nearly 500 stars for which the IRFM was used to determine temperatures was presented in Alonso, Arribas, & Martinez-Roger (1996a). Bonifacio and Molaro used these temperatures (1997) to accurately determine Li abundances in 41 plateau stars as a follow-up of their previous work using Balmer line temperatures (Molaro, Primas, & Bonifacio 1995). For Li similar results were found for the plateau abundance in each of the two methods. In Alonso, Arribas, & Martinez-Roger (1996b), calibrated expressions for the effective temperatures were derived based on the earlier tabulation. Unfortunately, these calibrations do not always lead to the same temperatures found in the

tabulations and differences by as much as 200 K occur. We will present results based on both (1) the IRFM temperatures in the compilation Alonso, Arribas, & Martinez-Roger (1996a), and (2) based on the calibration.

We can not overly stress the importance of reliable stellar data. The Balmer-line data appear to be self-consistent, and are probably the most reliable. However, because we will present results based on the IRFM temperature scales, we would like to point out that there are significant differences in the data. To illustrate the point we take for example the case of the star BD 3° 740. From Axer *et al.* (1994), we find this star to have ($T_{\rm eff}, \ln g$, [Fe/H]) = (6264, 3.72, -2.36). The beryllium and oxygen abundances for this star was reported by Boesgaard *et al.* (1999b) and (1999a). When adjusted for these stellar parameters, we find [Be/H] = -13.36, and [O/H] = -1.74. In contrast, the stellar parameters from Alonso *et al.* (1996a) are (6110,3.73,-2.01)[2] with corresponding Be and O abundances of -13.44 and -2.05. Garcia-Lopez *et al.* (1998) use a calibrated IRFM based on Alonso *et al.* (1996b) and take (6295,4.00, -3.00). For these choices, we have [Be/H] = -13.24 and [O/H] = -1.90. Notice the extremely large range in assumed metallicities and the difference in the two so-called IRFM temperatures. While this may not be a typical example of the difference in stellar parameters, it is differences such as this (and this star is not unique) that accounts for the difference in our results and the implications we must draw from them.

We also note that in addition to the large systematic differences in the Fe abundances (an order of magnitude in the above example), it has recently been argued that NLTE effects for Fe, particularly in low metallicity stars are non-negligible (Thévenin & Idiart 1999). At the low end of the metallicity range considered here, they argue for a ~ 0.3 dex upward correction in [Fe/H]. We have not included this correction in the data discussed below.

In the next section we will fit the BeB-OFe abundances over Pop II metallicities. The fits span a metallicity range $-3 \lesssim$ [Fe/H] $\lesssim -0.8$, and $-2 \lesssim$ [O/H] $\lesssim -0.5$ depending on the particular choice of stellar parameters. The upper bounds roughly mark the disk-halo transition, and the low metallicity bounds are just set by the availability of BeB data.

As we indicated, we will consider three sets of stellar parameters to be used in the BeB vs OFe analysis. The three are: stellar parameters based on the Balmer line data of Axer *et al.* (1994) – to be denoted as Balmer; the IRFM, with data from Alonso *et al.* (1996a) – denoted as IRFM1; the IRFM with stellar parameters as determined from the calibrations in Alonso *et al.* (1996b) as reported by Garcia-Lopez *et al.* (1998) and Israelian *et al.* (1998) – denoted as IRFM2. Note that at low metallicities this calibration is based on an analytic formula which is divergent. Thus, the points at low metallicity could be questionable. Be abundances used in the present work are from Rebolo *et al.* (1988), Ryan *et al.* (1990, 1992), Gilmore *et al.* (1992), Rebolo *et al.* (1993), Boesgaard & King (1993), Primas (1995), Hobbs & Thorburn (1996), Molaro *et al.* (1997),

[2]The surface gravity was recalculated by Bonifacio & Molaro (1997)

Boesgaard *et al.* (1999b). For each star, and for each choice of Balmer, IRFM1,2, we first adjust the Be abundance to a common set of stellar parameters. Then when multiple observations for a given star are available these abundances are weight averaged. LTE is commonly used, since non-LTE (NLTE) corrections for Be are not expected to be significant. In total, we have data on Be for 37 stars. Not all of the stellar parameters have been determined in a uniform way for the entire set of 37 stars. In the case of the Balmer set, we have parameters from Axer *et al.* (1994) for 22 stars. This set can be enlarged somewhat using the data of Boesgaard *et al.* (1999b) who have presented results based on two scales, the King (1993) scale which they claim is similar to Balmer and Carney (1983) which they claim is similar to IRFM. Thus for Balmer + King we have data for 30 stars. In the case of IRFM1, we also have data on 22 stars. IRFM 1 + Carney contains 25 stars. Finally for IRFM2, there are only 18 stars, but IRFM2 + Carney gets us up to 24 stars.

B abundances are taken from Duncan *et al.* (1997) and Garcia-Lopez *et al.* (1998) and Primas *et al.* (1999). NLTE corrections for B are significant (Kiselman 1994, Kiselman & Carlsson 1996), and are not uniform over metallicity, giving larger enhancements at the lower metallicities. Thus, NLTE correction have the systematic effect of flattening the B-OFe trends. We apply the same procedure as described above for the boron data. There are a total of 15 low metallicity stars with boron measured, of which we have Balmer data for 11 (and Balmer + King on 13). 9 stars are known for IRFM1 (and 10 for IRFM1 + Carney), and 11 for IRFM2.

Table 1: Slopes for O/Fe versus Fe.

number	method	slope
22	Balmer	-0.48 ± 0.16
31	Balmer	-0.51 ± 0.10
36	Balmer	-0.47 ± 0.09
22	IRFM1	-0.45 ± 0.14
27	IRFM1	-0.44 ± 0.10
36	IRFM1	-0.43 ± 0.09
22	IRFM2	-0.35 ± 0.10
29	IRFM2	-0.36 ± 0.09
36	IRFM2	-0.32 ± 0.08

Pop II oxygen abundances, and O/Fe, are critical for all studies of nucleosynthesis. The long discussion of O abundances in the literature illustrates that the path from stellar spectra to abundances is not a trivial one. Three different lines have been used to obtain the oxygen abundances with varying results. These are: (1) the allowed O I triplet at 7774 Å; (2) the forbidden [O I] line at 6300 Å; and (3) molecular OH lines at 3085 Å. The third method was suggested by Bessell, Hughes & Cottrell (1984) and recently high resolution UV spectra were obtained for many of the stars with Be and B observations (Nissen *et al.* 1994, Israelian, García-López, & Rebolo 1998, Boesgaard *et al.* 1999a). These new data suggest a significant nonzero [O/Fe] trend (versus [Fe/H]) in Pop II stars. We use all of the recent data on OH lines and combine the data in a

similar manner as that described for Be. In the two most recent works, a strong case is made for a varying O/Fe at low metallicity. The results of these two groups are in excellent agreement. It should be noted that the forbidden line continues to show lower O/H abundances as claimed in the recent work of Fulbright & Kraft (1999).

For O/H, we have a total of 36 stars with low metallicity OH data. There are 22 stars with Balmer data, and 31 with Balmer + King. There are 22 stars with IRFM1 data and 27 with IRFM1 + Carney. There are also 22 IRFM2 O/H data points and 29 IRFM2 + Carney. We will define the logarithmic slope $\omega_{\rm O/Fe}$ for O/Fe vs Fe by

$$[{\rm O/Fe}] = \omega_{\rm O/Fe}[{\rm Fe/H}] + const \tag{1}$$

Our results for the slopes are given in Table 1. Within the uncertainties these slopes are all consistent with one another. The IRFM2 slopes are somewhat smaller and in very good agreement with those found by Israelian *et al.* (1998) as should be expected since the IRFM2 temperature scales are taken from that work.

3. Statistical Tests of BeB Origin

We will first derive the overall fits for BeB vs both O and Fe using the data discussed above. The Be and B data can be fit versus [Fe/H] or [O/H], using logarithmic abundances so that for example,

$$[{\rm Be}] = \omega_{\rm BeFe}\,[{\rm Fe/H}] \;+\; const \tag{2}$$

We will focus on the logarithmic slopes such as $\omega_{\rm BeFe}$; the same procedure, applied to boron, gives $\omega_{\rm BFe}$, etc. [Be] is defined as log(Be/H) + 12. Our results are summarized in tables below.

Note that there is a sharp difference in slopes of BeB vs Fe/H as compared with O/H. This is implied by the variability in O/Fe at low metallicity. Also note that for the cases of Balmer and IRFM1, the scaling of Be with respect to O/H is almost purely secondary. Boron, on the other hand shows a strong primary component, which in this case, we would expect to be due to the ν-process (Woosley *et al.* 1990, Olive *et al.* 1994). The IRFM2 data still indicates the need for an early primary Be component as we explain below.

We would also like to call attention to the slopes for B/Be with respect to either Fe/H or O/H. They are all non-zero (even when the relatively large uncertainties are taken into account), though there is a considerable dispersion in the data. This is a departure from the standard picture of purely secondary GCR nucleosynthesis as well more recent primary models of BeB nucleosynthesis. This behavior is due in part to the new Be observations of Boesgaard *et al.* (1999b) for some

Table 2: Slopes for Be versus Fe and O.

method	number	tracer	slope	number	tracer	slope
Balmer	22	Fe	1.39 ± 0.16	19	O	1.78 ± 0.19
Balmer	30	Fe	1.26 ± 0.11	27	O	1.79 ± 0.16
Balmer	37	Fe	1.27 ± 0.10	31	O	1.70 ± 0.17
IRFM1	22	Fe	1.23 ± 0.14	21	O	1.83 ± 0.19
IRFM1	25	Fe	1.19 ± 0.11	24	O	1.80 ± 0.17
IRFM1	37	Fe	1.21 ± 0.10	31	O	1.49 ± 0.14
IRFM2	18	Fe	1.18 ± 0.11	18	O	1.36 ± 0.09
IRFM2	24	Fe	1.15 ± 0.10	24	O	1.35 ± 0.08
IRFM2	37	Fe	1.18 ± 0.09	31	O	1.29 ± 0.08

Table 3: Slopes for B versus Fe and O.

method	number	tracer	slope	number	tracer	slope
Balmer	11	Fe	0.78 ± 0.22	10	O	1.23 ± 0.32
Balmer	13	Fe	0.56 ± 0.14	12	O	1.22 ± 0.28
Balmer	15	Fe	0.60 ± 0.14			
IRFM1	9	Fe	0.73 ± 0.19	9	O	0.98 ± 0.28
IRFM1	10	Fe	0.63 ± 0.13	10	O	0.94 ± 0.23
IRFM1	15	Fe	0.70 ± 0.10	12	O	1.00 ± 0.20
IRFM2	11	Fe	0.72 ± 0.14	11	O	1.02 ± 0.16
IRFM2	15	Fe	0.70 ± 0.11	12	O	1.00 ± 0.16

relatively low metalicity stars. There are now a few cases for which the B/Be ratio in fact exceed 100 as can be seen in the figures. This is true for all of the choices of stellar parameters considered. This in fact is a prediction of the secondary model with ν-process B production (Olive *et al.* 1994; Fields, Olive, & Schramm 1995).

We are now in position to test the BeB data for the presence of two components, primary and secondary. Because physically, BeB production is tied to elements such as CNO, for the data available, we analyze only the Be and B trends versus oxygen. For $A \in$ BeB, the data are fit to

$$\frac{A}{\mathrm{H}} = a_1 \frac{\mathrm{O}}{\mathrm{H}} + a_2 \left(\frac{\mathrm{O}}{\mathrm{H}}\right)^2 \tag{3}$$

$$= \left(\frac{A}{\mathrm{H}}\right)_\odot \left[\alpha_1 \frac{\mathrm{O/H}}{(\mathrm{O/H})_\odot} + \alpha_2 \left(\frac{\mathrm{O/H}}{(\mathrm{O/H})_\odot}\right)^2\right] \tag{4}$$

where the fit parameters a_i are expressed in "scaled" units $\alpha_1 = (\mathrm{O}/A)_\odot a_1$ and $\alpha_2 = (\mathrm{O/H})^2_\odot/(A/\mathrm{H})_\odot\, a_2$. Note that in eq. (3), the abundances are *not* logarithmic, but are the (linear) ratios with respect to hydrogen. The fit parameters a_1 and a_2 (equivalently, α_1 and α_2) quantify respectively the primary and secondary contributions to A. These are given in

Table 4: Slopes for B/Be versus Fe and O.

method	number	tracer	slope	number	tracer	slope
Balmer	9	Fe	-0.52 ± 0.24	9	O	-0.68 ± 0.37
Balmer	11	Fe	-0.57 ± 0.16	11	O	-0.91 ± 0.30
IRFM1	9	Fe	-0.49 ± 0.18	9	O	-0.81 ± 0.27
IRFM1	10	Fe	-0.59 ± 0.15	10	O	-0.96 ± 0.25
IRFM1	11	Fe	-0.60 ± 0.15	11	O	-0.71 ± 0.20
IRFM2	10	Fe	-0.57 ± 0.14	10	O	-0.53 ± 0.21
IRFM2	11	Fe	-0.56 ± 0.14	11	O	-0.49 ± 0.20

Table 5.

Table 5: Break points for Be versus O.

number	method	α_1	α_2	$[O/H]_{eq}$
19	Balmer	0.042 ± 0.003	2.30 ± 0.70	-1.75
27	Balmer	0.027 ± 0.027	2.21 ± 0.49	-1.94
31	Balmer	0.027 ± 0.027	2.28 ± 0.52	-1.94
21	IRFM1	0.034 ± 0.034	2.14 ± 0.53	-1.79
24	IRFM1	0.031 ± 0.027	2.28 ± 0.51	-1.88
31	IRFM1	0.050 ± 0.031	2.14 ± 0.54	-1.62
18	IRFM2	0.111 ± 0.031	2.57 ± 0.76	-1.37
24	IRFM2	0.115 ± 0.031	2.61 ± 0.68	-1.36
31	IRFM2	0.122 ± 0.031	2.79 ± 0.70	-1.35

The terms in eq. (3) are equal at the metallicity

$$\left(\frac{\mathrm{O}}{\mathrm{H}}\right)_{\mathrm{eq}} = \frac{a_1}{a_2} = \frac{\alpha_1}{\alpha_2} \left(\frac{\mathrm{O}}{\mathrm{H}}\right)_{\odot} \tag{5}$$

with the primary term dominating at $\mathrm{O/H} < (\mathrm{O/H})_{\mathrm{eq}}$, and the secondary term dominating at $\mathrm{O/H} > (\mathrm{O/H})_{\mathrm{eq}}$. Physically, $(\mathrm{O/H})_{\mathrm{eq}}$ identifies the epoch at which primary cosmic ray sources are overcome by secondary sources; we thus refer to this as the "break point" of the A-O trend. These points (in [O/H]) appear as $[\mathrm{O/H}]_{\mathrm{eq}}$ in Table 5, and indicate the metallicity at which the transition from primary to secondary should occur. Recall that any primary component present will be dominant at sufficiently low [O/H]. Therefore we can use the information in the table to compare the relevant strengths of the primary and secondary components and constrain models for cosmic ray origin and acceleration. As one can see, for both Balmer and IRFM1, the break point occurs at very low [O/H], in fact at the edge of data as can be seen from the figures where the data is plotted.

There is also the question regarding how meaningful these two-parameter fits are. To give a

quantitative answer to this question requires an examination of the χ^2 of the various fits in Table 5. In Table 6, we show the relevant χ^2's for the break point fits together with those for fits where either α_1 or α_2 are forced to be 0. That is the χ^2 for either a purely linear or purely quadratic evolution.

Table 6: χ^2 for the break points in Table 5.

number	method	χ^2	$\chi^2(\alpha_1 = 0)$ (P_F)	$\chi^2(\alpha_2 = 0)$ (P_F)
19	Balmer	18.4	20.2 (78%)	30.9 (99.6%)
27	Balmer	27.2	28.3 (68%)	54.1 (99.99%)
31	Balmer	34.1	35.3 (68%)	61.2 (99.99%)
21	IRFM1	13.8	15.0 (68%)	30.7 (99.99%)
24	IRFM1	18.1	19.4 (78%)	39.6 (99.99%)
31	IRFM1	34.4	39.1 (94%)	53.1 (99.96%)
18	IRFM2	24.2	56.4 (99.97%)	46.6 (99.8%)
24	IRFM2	29.5	61.8 (99.99%)	54.0 (99.97%)
31	IRFM2	40.0	72.7 (99.99%)	65.7 (99.98%)

In order to justify an additional parameter, we must find a significant drop in the χ^2. The degree of significance can be quantified by the F-test, which produces a likelihood that the 2-parameter fit is a better description of the data than the 1-parameter (primary or secondary) fit. This quantity is also shown in the Table 6 as P_F. For example, in the first line of that table, for the Balmer case with 19 points, we see that while the 2-parameter fit is clearly superior (with a probability of 99.6%) to a straight primary (linear) fit, it is only an improvement at the 78% level over a purely secondary fit. That is, in the latter case, it should be questioned whether or not the 2-parameter fit is actually better than a purely secondary (quadratic) fit. This pattern is similar for the IRFM1 data set as well. In contrast, for the IRFM2 data, the 2-parameter fit is clearly preferred to either the purely primary or secondary fits.

Before concluding this section, we note that use of Fe abundances to study the BeB evolution presents us with several difficulties. In addition to the overall uncertainties in the observational determination of [Fe/H] (with or without NLTE effects), we will also find it difficult to model the recently observed O/Fe slopes. In section 4.4, we note that most calculated yields predict an overabundance of Fe with respect to O, particularly for large stellar masses, when compared with the recent observations. There is however, a substantial uncertainty in the ejected yield of Fe relative to the mass of Fe trapped in the stellar remnant. For this reason, it has been suggested (Shigeyama & Tsujimoto 1998) that the use of Mg instead of Fe should be a reliable tracer for chemical evolution studies. Indeed, there have been some recent preliminary observational attempts (Fuhrmann *et al.* 1997, Fuhrmann 1998) to obtain Mg data for the halo stars of interest. In this context, it happens that Mg is less affected by spectroscopic uncertainties than O; as such Mg might be a better metallicity tracer than either O and Fe.

4. Models

Using the results of the BeB fits, we can now test different scenarios for their non-thermal, spallative nucleosynthesis. To compute the BeB-OFe trend expected for each scenario, one must combine models for cosmic ray/accelerated particle origin, particle propagation, and chemical evolution. We describe these in turn.

4.1. Cosmic Ray Sources

We focus on two suggestions for the origin of accelerated particles:

1. Standard GCR, which leads to secondary Be and B trends (proportional to O^2).
2. Superbubble accelerated particles (SAP). The metal-enriched composition of the superbubbles is reflected in the particles and leads to primary Be and B production (proportional to O).

For each of these, we must specify the source spectrum $Q(E) \equiv dN/dE$ of the accelerated particles, their composition, and the dependence of the composition on that of the ambient medium. For further discussion see Vangioni-Flam, Cassé, & Audouze (1999).

4.1.1. Standard Galactic Cosmic Rays

For many years it has been a common perception that supernova remnants are the principal, perhaps predominant, agents which accelerate galactic cosmic rays up to an energy of around 10^{15} eV. Supernova remnants have the energy necessary to satisfy the cosmic ray energetics requirement if their acceleration efficiency is about 0.1; the current estimate of supernova rates in our Galaxy can adequately supply the observed cosmic ray density. Such cosmic rays are presumed to be energized by diffuse shock (Fermi) acceleration, the shock itself being induced by the impact of the supernova ejecta on the surrounding interstellar medium (e.g., Ellison, Drury, & Meyer 1997).

We follow here the standard approach, which assumes that supernova blast waves create strong shocks which accelerate ISM material, with a composition that retains certain biases. Specifically, the model follows very closely that of Fields & Olive (1999a), but is also similar to that of Lemoine *et al.* (1998). Since the acceleration engines are supernovae, the source intensity scales as the supernova rate and thus (for all but the earlies times) the star formation rate: $Q(t) \propto \dot{N}_{\rm II}(t) \sim \psi(t)$. Note that in the early Galaxy, Type II supernovae dominate.

The source spectrum is that of particles accelerated by strong shocks. To a good approximation (e.g., Ellison, Drury, & Meyer 1997), this gives a power law in momentum, of the form $dN/dp \propto p^{-2}$. In energy space, we have $Q(E) = dN/dp\ dp/dE$, which goes to $q(E) \sim E^{-1.5}$ at low energies, and $q(E) \sim E^{-2}$ at high energies. Of course, the full, relativistic $p(E)$ expression

is used for all energies in the numerical work. The proton source spectrum appears in Figure 1a. This propagated spectrum (see Figure 1b) is consistent with the one determined on the basis of a refined propagation model fitting a large number of observations by Strong & Moskalenko (1998).

The accelerated particle composition in species i reflects that of the ISM:

$$y_i^{\rm CR}(t) \equiv Q_i(t)/Q_p(t) \propto X_i(t) \tag{6}$$

with the following scaling. The present-day observed cosmic-ray source composition, $y_i^{\rm CR}(t_0)$, differs from a solar (and ISM) composition in that refractory and/or low first ionization potential elements are enhanced with respect to the volatile and/or high ionization potential ones (Meyer, Ellison, & Drury 1997, Cassé and Goret 1978, Vangioni-Flam and Cassé 2000). For example, oxygen has a cosmic ray abundance $y_{\rm O}^{\rm CR,0} = 3.5 \times 10^{-3} = 4.1{\rm O/H}_\odot$ which is enhanced over that of the ISM, while helium is relatively depleted: $y_\alpha^{\rm CR,0} = 0.067 = 0.69{\rm He/H}_\odot$. Thus we use the present-day cosmic-ray abundances in the scaling rule for the source particles:

$$y_i^{\rm CR}(t) = \frac{X_i(t)}{X_{i,\odot}}\ y_i^{\rm CR}(t_0) \tag{7}$$

This scaling has the desired properties that $y_i(t) \propto X_i(t)$, and that $y_i^{\rm CR}(t) = y_i^{\rm CR}(t_0)$ when $X_i(t) = X_{i,\odot}$.

4.1.2. Superbubble Accelerated Particles

An accelerated particle component in addition to the GCRs has been proposed utilizing i) individual massive exploding stars (Cassé *et al.* 1995) and ii) collective explosions in superbubbles. These are large regions of rarefied, ionized, metal-rich gas associated with star formation regions. Observationally, superbubbles are identified by their dense shells of neutral gas. The regions interior to these shells are devoid of neutral gas, but sometimes show evidence of ionized gas. Superbubbles probably play a fundamental role in the structure and energetics of star-forming regions, and of the ISM in general; for a review see, e.g., Spitzer (1990), Tenorio-Tagle & Bodenheimer (1988), MacLow and Mc Cray (1988), Walker *et al.* (1998).

The structure and dynamics of superbubbles make them favorable sites for particle acceleration. The collective effects of massive stars which sweep material out into the dense shells, leaving behind hot, rarefied interiors. The copious injection of matter and energy by massive stars provides the ingredients of a powerful ion accelerator. Ejecta from core collapse supernovae generate recurrent but weak shock waves, and turbulence. These shocks act as accelerators within the superbubble environment. Moreover, these regions provide a large energy reservoir: they have the necessary power (10^{52} ergs and higher) and size to energize a great number of low energy particles.

Superbubble accelerated particles (SAP) generated this way could be a significant a Galaxy-wide component of non-thermal particles (Vangioni-Flam *et al.* 1996, 1998). The SAP's

would have a metal-rich composition reflecting that of the superbubbles. According to recent calculations by Bykov (1999), the SAP energy spectrum is not very different from that of GCR's (but other spectral shapes are possible). The SAP's would inevitably produce BeB over to the long duration of massive star activity in the parent OB associations ($10^5 - 10^7$ yr), and thus are likely to be a significant BeB source. The production of BeB in superbubbles, as well as gamma-rays and X-rays (Vangioni-Flam, Cassé, & Audouze 1999) is thus well-motivated. The existence of these particles can be confirmed by gamma-ray line observations that will be performed by the European INTEGRAL satellite. One could even turn the problem around, and use constraints on primary BeB to probe the nonthermal component and physical conditions in superbubbles.

The study of the particle acceleration in superbubbles is only in its infancy. Much remains to be explored, including the relation between the parent molecular clouds and their stellar products, the structure and distribution of the environment and its degree of ionization, and the parameters of the shocks. All of these will affect the composition and the energy spectrum of the accelerated particles.

The spectrum, $\phi_{\rm SB,int}$, of energetic particles *within* the rarefied superbubble interior has been studied in considerable detail (Bykov 1999). Due to the low densities of these regions, nuclear interactions are slow and thus BeB production in the interiors is negligible. The dominant BeB synthesis instead occurs as the particles escape from the interiors and traverse the dense shells. Thus, in deriving BeB production rates, the interior flux, $\phi_{\rm SB,int}$, becomes the *source* for the particle flux within the shells surrounding them. That is, $Q_{\rm SB,shell} \propto \phi_{\rm SB,int}$. For the $\phi_{\rm SB,int}$, we use a simple analytic form which closely follows Bykov's (1999) $\zeta = 0.1$ model. The source spectrum appears in Figure 1a. As one can see, it does not differ substantially from the GCR source spectrum.

The energetic particle composition reflects that of the superbubble interior, and thus is highly enriched in supernova products. To model this, we take the particle composition to be time-independent in the early Galaxy. We take the superbubble abundances to be the same as the ejecta of massive stars with primordial $Z = 0$ composition. Specifically, we set the composition to be that of a $40M_\odot$ star, Woosley & Weaver's (1995) model U40B. The particles are thus highly enriched (relative to solar) in O ($y_{\rm O}^{\rm SB} = 32{\rm O/H}_\odot$), and also enriched in He and C.

4.2. Cosmic Ray Propagation

We begin with a transport equation which describes the propagation and deceleration of nuclei from their sources through the ISM. This equation is a general one, and can be applied to both GCR and SAP components. Once launched in space, accelerated nuclei are deviated by the magnetic field irregularities and lose memory of their origin. The particles propagate diffusively throughout the Galaxy. As they traverse the ISM, they suffer ionization energy losses and undergo nuclear interactions. For the lower energy particles, ionization losses are important

and the distances traversed are short. High energy nuclei, however, traverse complicated paths whose length is much larger than the thickness of the Galaxy. Each time they reach the border of the Galaxy (badly defined) the particles have a small probability of escape. The Galaxy in this context is like a "leaky box," and we will describe cosmic ray propagation via the leaky box model. Here we briefly summarize this model, which is discussed in detail in the context of BeB nucleosynthesis by, e.g., Prantzos, Cassé, & Vangioni-Flam (1993) and Fields, Olive, & Schramm (1994).

The leaky box propagation equation can be expressed as

$$\frac{\partial}{\partial t}N(E) = Q(E) - \frac{1}{\tau}N(E) + \frac{\partial}{\partial E}\left[b(E)\,N(E)\right] \stackrel{\rm SS}{=} 0 \tag{8}$$

where the last equality assumes a steady state. The source (injection) spectrum $Q(E)$ depend on the cosmic ray model, as discussed in the preceding sections. Coulomb interactions with ambient electrons lead to an ionization energy loss rate $b(E)$. The escape time, τ, is the harmonic mean of the confinement time and the nuclear destruction time. The energy distribution is modified in the course of the propagation since energy losses are energy dependent.

Dividing by the mean density of the ISM one gets

$$\frac{\partial}{\partial X}\phi(E) = q(E) - \frac{1}{\Lambda}\phi(E) + \frac{\partial}{\partial E}\left[\omega(E)\,\phi(E)\right] \stackrel{\rm SS}{=} 0 \tag{9}$$

with $\omega(E) = dE/dX$, in MeV/(g cm^{-2}). The equilibrium spectrum, ϕ, is solution of this equation. BeB production rates and ratios are obtained by integrating over this spectrum rather than the source spectrum q. Propagated spectra for GCR and SAP models appear in Figure 1b.

The production rate of $\ell \in$ BeB per unit volume is

$$\frac{d}{dt}n_\ell = \sum_{ij} n_i \int\, dE\ \sigma_{ij}^{\ell}(E)\ \phi_j(E)\ S_\ell(E) \tag{10}$$

Here n_i is the ISM number density of species i, $\phi_j(E)$ is the solution to eq. (9) for particle species j, and $\sigma_{ij}^{\ell}(E)$ is the cross section for the spallation reaction $i + j \to \ell + \cdots$ (Read & Viola 1984). The factor $S_\ell(E) = \exp[-R_\ell(E)/\Lambda]$ is the probability that the daughter nucleus ℓ is stopped and thermalized in the ISM before it can escape from the Galaxy.

4.3. Neutrino Process

The neutrino process (Woosley *et al.* 1990) provides a means for direct (primary) ^{11}B production in supernovae. As the large neutrino flux streams from the supernova core, it traverses the overlying shells of material. When the flux passes through the carbon shell, some of the neutrinos collide inelastically with the ^{12}C nuclei, and make ^{11}B spallatively, by removing a nucleon: $^{12}\mathrm{C} + \nu \to {}^{11}\mathrm{B} + p + \nu'$. Other inelastic reactions create ^{10}B and ^{9}Be, but these species

do not survive the subsequent passing of the blast wave. Thus, the ν-process provides an elegant, primary source of ^{11}B, but does not make Be.

We adopt the ν-process yields of Woosley & Weaver (1995), who found that ^{11}B is made at significant levels. The precise yields, however, depend on the neutrino temperature, and hence are uncertain. Although the ^{11}B production is very sensitive to the temperature, the relative yields for different mass supernovae are probably better known. To allow for this uncertainty, we follow previous work (Olive *et al.* 1994; Vangioni-Flam *et al.* 1996; Fields & Olive 1999a) in taking the ν-process yields to be uncertain by an overall factor. We thus write $m_{ej,11}(m) = f_\nu m^{\rm WW}_{ej,11}(m)$, where the yield $m_{ej,11}$ of ^{11}B is a function of progenitor mass m, and scales with the Woosley & Weaver yield $m^{\rm WW}_{ej,11}(m)$. The scale factor f_ν will be set by a fit to the data, as described below, and the resulting value amounts to a constraint on the neutrino temperature.

4.4. Chemical Evolution

The production of BeB depends on the intensity and composition of both GCR and SAP, as well as the ISM composition and gas mass. These quantities are time dependent, and to follow their evolution requires a model of Galactic chemical evolution. The chemical evolution model adopted here is described in detail in Fields & Olive 1999a, so we will only summarize the key points.

For the star formation rate $\psi(t)$ we adopt $\psi = \lambda M_{\rm gas}$, with $\lambda = 0.3\,{\rm Gyr}^{-1}$; our results are insensitive to the details of ψ. We use a power law initial mass function, $\phi \propto m^{-2.65}$, with $m \in (0.1 M_\odot, 100 M_\odot)$. For simplicity we use a closed box model, i.e., without infall or outflow. We account for different stellar lifetimes as a function of mass, and thus we do not use the instantaneous recycling approximation.

The elements evolved in the code are H, He, C, N, O, and Fe, as well as BeB. The high mass (Type II supernova) yields are from Woosley & Weaver (1995). The intermediate mass (AGB) yields are from van den Hoek & Groenewegen (1997). In both cases, the full metallicity dependence of the tabulated yields is used.

The different roles of O and Fe deserve mention. We stress that the oxygen yields are the most critical, since as we have argued O is the better diagnostic for BeB origin, and thus the BeB-O trends are the main focus throughout this paper. The adopted O yields of Woosley & Weaver (1995) are in broad agreement with the work of Thielemann, Nomoto, & Hashimoto (1996). Furthermore, the O yields are not strongly altered in explosive nucleosynthesis, nor are they sensitive to the mass cut.

The yields of iron, on the other hand, are much more uncertain. However, because Fe has been shown in all previous work, we also will show this for comparison. Our treatment of Fe production follows that of Fields & Olive (1999a), and is driven by the new O/Fe data, The observed O/Fe-Fe

relation (eq. 1) is key to interpreting the BeB-Fe slopes, so we adopt this relation, and solve for iron:

$$\mathrm{Fe/Fe_\odot} \propto (\mathrm{O/O_\odot})^{1/(1+\omega_{\mathrm{O/Fe}})} \tag{11}$$

Since O yields and evolution are fixed in the model, this strategy amounts to fixing the effective yield for Fe. Note that the non-constancy of O/Fe (i.e., $\omega_{\mathrm{O/Fe}} \neq 0$) demands that the derived Fe yield is not proportional to the O yield.

In other words, we can derive the effective Fe yields needed to agree with the O/Fe data and the O yields. The effective Fe yield $\langle m_{\mathrm{ej,Fe}} \rangle$ is the mean Fe mass ejected per supernova, which is the total Fe ejection rate divided by the supernova rate:

$$\langle m_{\mathrm{ej,Fe}} \rangle \equiv \frac{E_{\mathrm{Fe}}}{\dot{N}_{\mathrm{II}}} \tag{12}$$

The iron mass ejection rate can be inferred as follows. The usual chemical evolution expressions give $E_{\mathrm{Fe}} = M_g \dot{X}_{\mathrm{Fe}} + E X_{\mathrm{Fe}}$. We compute $\dot{X}_{\mathrm{Fe}}$ via eq. (11), which is imposed via $\dot{X}_{\mathrm{Fe}}/X_{\mathrm{Fe}} = (1+\omega_{\mathrm{O/Fe}})^{-1} \dot{X}_{\mathrm{O}}/X_{\mathrm{O}}$, where $\dot{X}_{\mathrm{O}}$ is computed as usual from the high-mass yields within the model. Thus $\langle m_{\mathrm{ej,Fe}} \rangle$ is an effective yield, averaged over the mass function, at each epoch t.

Figure 2 shows the time evolution of $\langle m_{\mathrm{ej,Fe}} \rangle$, and for comparison, a similar effective yield for O. At any give time, the mass range includes all of those stars whose mass m is larger than m_t, the mass whose lifetime $\tau(m) = t$. Thus, the average includes an increasingly larger mass range of stars as time goes on. We therefore also plot these results as a function of m_t in the lower panel of Figure 2. We see that the effective O yield starts high ($> 10 M_\odot$) when the progenitors have high mass, and then levels off at $10 M_\odot$, where the average then includes all supernovae. In contrast, Fe starts low and then builds up. Within the $m > 10 M_\odot$ regime, the Fe yield is not constant, but spans a large range, to include values at lower masses which are of the order of Fe yields estimated for observed supernovae, though somewhat lower than the yields of Woosley & Weaver (1995). Above 60 $M_\odot$, the Fe yield is assumed to be negligible. Below $m < 10 M_\odot$, $\langle m_{\mathrm{ej,Fe}} \rangle$ continues to rise to values approaching $1 M_\odot$. This rise thus coincides with the epoch when Type Ia supernovae should begin to contribute to iron enrichment. The Type Ia iron yields are expected to be nearly constant per explosion event, and to approach $1 M_\odot$; thus, one can view the $m < 10 M_\odot$ behavior of $\langle m_{\mathrm{ej,Fe}} \rangle$ as a measure of the increasing ratio of Type Ia/Type II supernova events.

It is noteworthy that the inferred Fe yields are at variance with the yields that Shigeyama & Tsujimoto (1998) inferred from Mg/Fe ratio in ultra-metal-poor halo stars (and from the light curves of supernovae, which however arise from a different population than the halo stars). While the trend in $\langle m_{\mathrm{ej,Fe}} \rangle$ is inferred from O/Fe to be decreasing with increasing progenitor mass, the trend inferred from Mg/Fe is found to do just the opposite. This difference is indeed striking but not surprising, since Shigeyama & Tsujimoto (1998) adopted a Mg/Fe relation that *decreases* towards low metallicity, rather than increases as O/Fe does. This result discrepancy indicates the need to get good observational constraints on the O-Fe-Mg relations.

An alternative model has been proposed in which the O/Fe relationship is obtained by assuming differential mixing of Be, O and Fe, the latter being locked up into grains (Ramaty and Lingenfelter 1999, Ramaty *et al.* 1999). With the nominal yields of Woosley and Weaver (1995), they obtain an acceptable O/Fe evolution at the expense of an additional free parameter: the mixing time.

5. Model Results

In presenting results, we will compare calculated Be and B trends with observations. In doing this, we focus on oxygen as a metallicity indicator. Using oxygen rather than iron has several theoretical advantages. Oxygen is a good tracer of the cosmic ray accelerators (Type II supernovae). Also, oxygen (and to a lesser extent C and N) provides the main raw material from which Be and B are carved by spallation. And while both oxygen and iron are both made by Type II supernovae, the oxygen yields are considerably less uncertain as they are dominated by well-understood hydrostatic burning processes, as opposed to the iron yield which depends sensitively on the details of the (poorly understood) explosion mechanism and mass cut. However, as noted above, Mg may be a promising evolutionary tracer: from the theoretical point of view, Mg shares the same robustness in prediced yields that O does, since it is not affected by the poor knowledge of the position of the mass cut between the neutron star and the supernova ejects on one hand; from the observational point of view, Mg abundances depends less on the details of the stellar atmospheric models (for instance it is less subject to NLTE effects, Fuhrmann (1998)).

5.1. Be and B Normalization

The three components in the BeB evolution lead to three free parameters:

1. The normalization of the GCR component. We scale the GCR flux via $\Phi(t) = f_{\rm GCR}[\psi(t)/\psi(t_0)]\Phi_0$, where the star formation rate scaling, $\psi(t)/\psi(t_0)$, is computed self-consistently in the model, and Φ_0 is the total flux in present-day cosmic rays, as in Figure 1.

2. The SAP (energetic particle) normalization. We put $\Phi_{\rm SAP}(t) = f_{\rm SAP}\Phi(t)$.

3. The ν-process normalization. The scaling f_ν is described in §4.3.

Each of the f_i are free, in that there are independent constraints on the normalizations, but we do have some independent constraints on their values. For example, the GCR normalization is essentially fixed by the present Galactic average GCR flux, which is constrained by GCR flux measurements in the vicinity of the earth at high energy (> 1 GeV) as well as by γ-ray observations (see Strong and Moskalenko (1999)). Thus, the GCR normalization is not arbitrary,

but on the other hand, since the present-day Galactic average flux is uncertain to within a factor of a few (Mori 1997). We find that the scaling is $f_{\rm GCR} = 2.1$, well within the uncertainties of the Galactic average GCR flux. Note that the other two normalizations are more poorly constrained; indeed, the BeB data are probably the best way to constrain them.

We thus need three pieces of data to fix the normalizations; then the resulting Be-B-O trends are predictions. This is done as follows

1. A break point $[{\rm O/H}]_{\rm eq}$ is chosen to match that of the data set being fit. This fixes the *relative* strength $f_{\rm SAP}$ of the GCR vs SAP components. Thus, the evolution of the species that have only GCR and SAP sources, namely Be and ^{10}B, are fixed up to an overall scale factor.

2. The Be evolution is normalized to reach $({\rm Be/H})_\odot$ at $({\rm O/H})_\odot$, which fixes $f_{\rm GCR}$. Thus Be-O is forced to have the right $[{\rm O/H}]_{\rm eq}$, and must go through the solar point.[3] We have now fixed the GCR and SAP components completely, only using the Be break point and solar point. In doing this, ^{10}B is completely determined, and ^{11}B is determined up to the ν-process contribution; both of these are *predictions* of the model.

3. Finally, the ν-process contribution to ^{11}B is scaled so that the predicted $^{11}{\rm B}/^{10}{\rm B}$ ratio agrees with the meteoritic value at solar metallicity; this fixes f_ν. Now the model is completely determined, and the scalings with O cannot be adjusted further.

Note that this procedure does *not* force elemental B to go through the solar point. As we will see, the models nevertheless *do* pass through or very near the solar point, which should be viewed as a success of the scenarios being tested.

5.2. Comparing Theory and Observation

To compare theory and observation we have run models following the procedure just described, and we now plot them with the observations for the different sets of stellar parameters.

As discussed above, the break point $[{\rm O/H}]_{\rm eq}$ is an input to the model. However, it is not an entirely free parameter, as is evident when applying a two-component (linear plus quadratic) fit to the Be-O points from the GCR model alone. We find that this model has a small but nonzero linear component, $\alpha_1 = 0.043$, in addition to the expected large quadratic term, $\alpha_2 = 3.8$ value. The small linear component results from the fact, shown in Fields & Olive (1999a), that the Be-O slope is slightly less than 2, due to small astration effects. This flattening leads to a small but

[3] Fortunately, the solar abundances of Be and B are now well established: there is now good agreement between the photospheric and meteoritic abundances of both beryllium and boron. After a long debate, the situation has finally been settled: Be and B are undepleted in the solar photosphere.

nonzero linear component in the fit. Because $\alpha_1 > 0$, the GCR model *alone* has a break point at -1.94, without any addition of the primary process. Thus, there is no way to arrange a break point below -1.94, since adding a purely primary component only raises the value of α_1 and thus the break point, defined by α_1/α_2.

In making the comparison between theory and observations, we have chosen the break point for each method corresponding to the *lowest* number of data points. This data subset uses stellar atmospheric parameters which have been derived directly from the prescription discussed, and therefore should be most free of systematic effects. For example, in the Balmer case, only 19 of the total 31 stars are truly what we have called Balmer. Recall an additional 8 were described as Balmer + King in section 2 and may have additional systematic effects entering which we are trying to avoid. This intermediate set (as well as the full data set) were used to compute slope values, etc., for comparison only.

The Balmer data have $[O/H]_{eq} = -1.75$ as given in (Table 5); the results of a BeB model with this $[O/H]_{eq}$ value appears in Figure 3. As it happens, this break point is close to that of the GCR component, and thus there is only a small SAP component for this model. Note that in this figure and those that follow, the SAP component and the GCR components cross at value of [O/H] below $[O/H]_{eq}$. This is due to the small primary component in the GCRs themselves ($\alpha_{1,GCR} = 0.043$), as discussed above. Thus $[O/H]_{eq}$ is determined by the sum of the two primary components, relative to the secondary component. One can see that the Be-O trend in this model fits the data quite well. The B-O model contains in addition the ν-process. The lower panel of Figure 3. plots the different components as well as the evolution of total abundance which sums the components. We see that B-O is dominated by the primary ν-process at low metallicity, and by the secondary GCR production at high metallicity, as expected. However, even at present the ν-process component is not negligible, being lower than the total GCR component by about a factor of 2 (as is indeed demanded by the fit to the $^{11}B/^{10}B$ ratio). We have scaled the ν-processyields of Woosley *et al.* (1990) downward by a factor of $f_\nu = 0.4$ here and, as it turns out, in the other models as well. This scaling also keeps the production of ^{7}Li small enough so as not to affect the Spite plateau as shown in Vangioni-Flam *et al.* (1996). In Figure 3, and in the figures that follow, the point shapes indicate which data sample the stars fall into (e.g., pure Balmer, Balmer + King, or full).

Figure 4 plots Be and B versus O for IRFM1, which has a break point $[O/H]_{eq} = -1.79$. The upper panel shows Be-O, and is very similar to the Balmer case discussed above due to the similarity in the break points. Again, the intrinsic linear portion of the GCR component influences the break point, which is why the break point is higher than the metallicity at which the GCR and SAP components are equal. The quality of the Be-O fit is clearly good. In the case of B-O (lower panel), the ν-process contributes as well, leading to a GCR dominance at a higher metallicity than for Be-O. Unlike Be-O, the B-O fit now seems to be a poor one. The overall shape is fine, but the curve is clearly high.

Figure 5 plots BeB-O evolution for IRFM2, which has $[O/H]_{eq} = -1.37$. In this case, the

transition from SAP dominance at low metallicity to GCR dominance at high metallicity is evident. The results here are qualitatively similar to the IRFM1 case: the Be-O evolution is satisfactory, while the B-O evolution seems high.

In the next set of figures, we show plots of B/Be versus O. At the lowest metallicity in the Balmer case, Be is secondary while B is dominated by the ν-process and is thus primary. Hence, the B/Be ratio changes as B/Be $\propto$ O^{-1} and has a log slope of -1, as seen in Figure 6. Interestingly, even with this rise, the model actually falls short of the two highest B/Be ratios, though the qualitative behavior is correct. At high metallicity, the GCR component dominates both Be and B, and the ratio flattens. In the IRFM case, at very low metallicity, both Be and B are dominated by the SAP component, and again the curve flattens. The behavior of B/Be for the other two cases are shown in Figure 7 (for IRFM1) and in Figure 8 (for IRFM2). In the latter case the break point is higher and thus there is only a narrow range in [O/H] where B/Be drops, and so the overall change in B/Be is smaller.

In the IRFM1 case, B/Be is also far from the very high B/Be data points at the lowest metallicities. This illustrates the power of the B/Be ratio to constrain the models. The data is still poor however. While the situation is presently too uncertain to clearly exclude the models presented, it is clear that more B/Be data at low metallicity will play a decisive role in determining Be and B origins.

In Table 7, we show the production ratios of GCR and SAP at solar metallicity. That these are so close traces back to the very similar energy spectra (in spite of their different composition).

Table 7: Production ratios for GCR and superbubble accelerated particles (SAP)

Ratio	Present ($Z = Z_\odot$) GCR	SAP
^{6}Li/^{9}Be	5	5.8
^{10}B/^{9}Be	5	4.9
^{7}Li/^{6}Li	1.4	1.2
^{7}Li/^{9}Be	7	6.8
^{11}B/^{9}Be	12	11.7
^{11}B/^{10}B	2.5	2.4
Li/Be	12	14
B/Be	17	16.6

5.3. Energetics

As emphasized by Ramaty *et al.* (1997, 1999), a study of the energy budget associated with BeB production models can give additional insight. There are several ways to proceed, but the key point is to link the energy in accelerated particles required to make the BeB with the available

energy budget in the form of supernovae. The power of the analysis is in judging whether the energy requirement changes with metallicity (and thus epoch); in particular, it is important to see whether there is too large an energy requirement in Population II.

We find that there is not an energetics problem in the models we consider. One way to see this is as follows. Given a model, we wish to compute the accelerated particle energy input per supernova:

$$\varepsilon_{\rm CR} = \frac{\dot{\mathcal{E}}_{\rm CR}}{\dot{N}_{\rm SN}} \tag{13}$$

where $\dot{\mathcal{E}}_{\rm CR}(t)$ is the total energy going into particle acceleration throughout the Galaxy per second, and $\dot{N}_{\rm SN}$ is the supernova rate. The direct approach is simply to note that in both the GCR and primary components, supernovae are the power source of energetic particles: $\dot{\mathcal{E}}_{\rm CR} \propto Q \propto \dot{N}_{\rm SN}$. Since the power input is proportional to the supernova rate, their ratio $\varepsilon_{\rm CR}$ is constant, independent of metallicity. The models always require the same accelerated particle energy per supernova. Note that this approach simply examines the internal consistency of the model. We have not used the properties of the Be data.

We can use the data, however, and get the same conclusion. One can derive the $\varepsilon_{\rm CR}$ scaling *observationally* by relating the Be-O and Be-Fe data to the energy budget. This comes about by using the definition of $\varepsilon_{\rm CR}$ above (eq. 13) and a "chain rule" expansion:

$$\left(\varepsilon_{\rm CR}\right)_{\rm obs} = \left(\frac{\dot{\mathcal{E}}_{\rm CR}}{\dot{M}_{\rm Be}}\right)_{\rm model} \left(\frac{\dot{M}_{\rm Be}}{\dot{M}_Z}\right)_{\rm obs} \left(\frac{\dot{M}_Z}{\dot{N}_{\rm SN}}\right)_{\rm model} \tag{14}$$

for the metal tracers $Z \in {\rm O, Fe}$. As we have indicated, the first and last terms must be taken from the model (note that in Pop II, $\dot{\mathcal{E}}_{\rm CR}/\dot{M}_{\rm Be} \simeq W/Q(Be)$ in the Ramaty *et al.* 1997 notation). The middle term can be related to the data, since $\dot{M}_{\rm Be}/\dot{M}_Z \propto {\rm Be}/Z$ as long as Be can be expressed as a power law in Z. All theory terms (both denominators and numerators) are individually calculable, so we can now rearrange terms:

$$\left(\varepsilon_{\rm CR}\right)_{\rm obs} = \left(\frac{\dot{\mathcal{E}}_{\rm CR}}{\dot{N}_{\rm SN}}\right)_{\rm model} \left(\frac{\dot{M}_{\rm Be}}{\dot{M}_Z}\right)_{\rm obs} \left(\frac{\dot{M}_Z}{\dot{M}_{\rm Be}}\right)_{\rm model} \tag{15}$$

$$\propto \frac{\left({\rm Be}/Z\right)_{\rm obs}}{\left({\rm Be}/Z\right)_{\rm model}} \tag{16}$$

Equation (16) follows from eq. (15) due to the intrinsic constancy of $\dot{\mathcal{E}}_{\rm CR}/\dot{N}_{\rm SN}$ in the models; now, however, something new has been added in that the observed Be/Z ratio appears explicitly. In particular, we see that the scaling of $\varepsilon_{\rm CR}$ with metallicity depends on the ratio of observed to predicted Be/Z. If the observations are well matched by the predictions, then the ratio remains constant, as does $\varepsilon_{\rm CR}$. In other words, the constancy of $\varepsilon_{\rm CR}$ is determined by the goodness of the Be-Z fit. Thus, *all models which fit the data are able to avoid an energetics problem.* This applies quite generally, to the models presented here as well as others (e.g., Ramaty *et al.* 1999) which fit

the data.[4]

This argument shows that the models in question are energetically sound, simply due to their agreement with the data; however, a more detailed analysis is instructive. As we have argued, it is preferable to use the O data as the metal tracer Z, as this is the most direct diagnostic of BeB origins. As we have emphasized, and shown in Table 2, the observational data clearly show that Be/O is not constant, but rather $(\mathrm{Be/O})_{\mathrm{obs}} \sim \mathrm{O}^{0.8\pm0.2}$, where the exact power depends on the atmospheric model used. This factor alone would lead to a *decrease* in $\varepsilon_{\mathrm{CR}}$ at low metallicity. However, when the GCR is dominant over SAP's, (i.e., for metallicities $[\mathrm{O/H}] > [\mathrm{O/H}]_{\mathrm{eq}}$), the "production efficiency" factor scales as $\dot{\mathcal{E}}_{\mathrm{CR}}/\dot{M}_{\mathrm{Be}} \sim \dot{N}_{\mathrm{SN}}/(\mathrm{O}\dot{N}_{\mathrm{SN}}) \sim \mathrm{O}^{-1}$. This reflects the reduced efficiency for GCR Be production in the early Galaxy: the paucity of O targets in the early ISM leads to a lower BeB production for each supernova's complement of accelerated particles; this factor alone would lead to an *increase* in $\varepsilon_{\mathrm{CR}}$. Thus, the first two factors in eq. (14) offset each other, which is largely why $\varepsilon_{\mathrm{CR}}$ is constant.

We must consider several smaller and more subtle effects to complete our analysis of eq. (14). The last factor in eq. (14), the "average yield" $\dot{M}_Z/\dot{N}_{\mathrm{SN}}$ has a weak dependence on O, rising slightly towards low metallicity. However, we have until now assumed that $\dot{M}_{\mathrm{Be}}/\dot{M}_Z \propto (\mathrm{Be}/Z)_{\mathrm{obs}}$. This is a good approximation in Pop II, where Be evolution is dominated by production only, i.e., $\dot{M}_{\mathrm{Be}} \sim Q(\mathrm{Be})$. But in Pop I, astration effects become important since many low-mass stars begin to die and return their astrated, Be-free gas, which dilutes the ISM Be abundance. Astration manifests itself in the Be-O and Be-Fe relations by the turnover of Be at high metallicity: Be production is overtaken by destruction. Thus, for Pop I, the change in Be gas mass is lower than the cosmic ray production term would give: $\dot{M}_{\mathrm{Be}} < Q(\mathrm{Be})$. Pop I Be production is, in this respect, less efficient than in Pop II where astration is small and $\dot{M}_{\mathrm{Be}} \simeq Q(\mathrm{Be})$. Thus, the Be-$Z$ relation is flattened in Pop I, and the extrapolation of $\varepsilon_{\mathrm{CR}}$ via eq. (14) back to Pop II overestimates the energy needed if this astration is neglected. Finally, at very low metallicity, $[\mathrm{O/H}] \lesssim [\mathrm{O/H}]_{\mathrm{eq}}$, the SAP component takes over the energy budget. Thus, just as SAP's are primarily responsible for BeB production below $[\mathrm{O/H}]_{\mathrm{eq}}$, they are also the dominant energy source in this range.

Finally, we consider using $Z = \mathrm{Fe}$ in eq. (14). To reiterate, the question regarding the energetic problem, rests on $\varepsilon_{\mathrm{CR}}$. This quantity may be constant, even though $W/Q(\mathrm{Be})$ is not constant, depending on the observed Be/Fe ratio and the ratio of Be/Fe produced. Since the Be-Fe slopes are larger than (though close to) 1, Be/Fe increases with Fe. More significantly, the Be/Fe production ratio does not scale as Fe itself, but rather $\dot{M}_{\mathrm{Be}} \propto O$ and $\mathrm{O} \sim \mathrm{Fe}^{0.5}$. Similarly, the iron yield per supernova may also not be constant if the yield of Fe falls off at large stellar masses (see Fig 2). Both of these facts simply reflect the fact that O/Fe is not constant in Pop II. Thus, models in which $W/Q(Be)$ is not constant, can not a priori be disregarded.

[4]Strictly speaking, the scaling argument we have given says that models which do not have an energetics problem at the *present epoch* and fit the Be/Z data will also satisfy the energy requirements in earlier epochs.

6. Conclusions

The history of the accelerated particles within the Galaxy is coded in the evolution of spallogenic Be and B. Recent theoretical studies of particle acceleration suggest that the Galaxy may have two components of nonthermal particles. These two populations yield different BeB evolution, GCR particles lead to secondary ($\propto$ O^2) production, while nuclei accelerated in superbubbles give a primary ($\propto$ O) production.

We have searched for the corresponding evidence of two components in the evolution of Be and B versus O and Fe abundances in low metallicity halo stars. Specifically, we have made two-component fits of abundance data, to identify the presence of primary and secondary BeB components, and to quantify their relative strength. This analysis has been carried out using consistent stellar atmosphere parameters based on Balmer lines and the infrared flux method (IRFM). Some results depend on the method used to get the atmospheric parameters, while others do not. In both Balmer and IRFM methods, the secondary BeB component is seen to dominate for [O/H] $\gtrsim -1.4$. However, the status of the primary component depends on the atmospheric parameters chosen. When the Balmer treatment is used, a primary mechanism is not required over the observed metallicities, whereas it is required in the IRFM2 case, where it dominates at [O/H] $\lesssim -1.4$.

We use the BeB-OFe fits to constrain the theories, whose predictions we model by combining cosmic ray nucleosynthesis and Galactic chemical evolution. The GCR component has the observed present-day spectrum, is assumed to be accelerated from supernovae, and to have a composition which scales with that of the ISM. For the case of superbubbles, the energy spectrum has been taken from Bykov (1999), and is quite similar to the that of the GCRs. Thus there a little hope to differentiate the two components on an isotopic basis, since the production ratios of superbubbles and GCR are very similar in spite of their different composition (C/O = 0.09 against C/O = 0.81 respectively). The two-component BeB-O fits constrain the models by demanding that: (1) the GCR production dominates over the superbubble component at [O/H] > -1.4 in all cases, and in the Balmer case it is unclear whether the SAP component is needed; (2) the secondary, GCR component requires that the mean GCR flux at present factor of 2.1 higher than current estimates; given the uncertainties, this is quite plausible; and (3) the ν-process is needed to produce ^{11}B, but at a level that is 40% of the fiducial Woosley & Weaver (1995) yields; again, this is well within the uncertainties of the yield calculations.

Our results can be further tested, and the constraints tightened, by several types of observations. Simultaneous and high signal/noise measurements of Be, B, O, and Fe, are called for. These must be interpreted within detailed and consistent atmospheric models including accurate NLTE corrections. The current situation is not definitive, since the conclusions regarding the primary component depend sensitively on the atmospheric parameters adopted. A critical goal is to determine Be and B abundances–as well as key ratios such as B/Be, Li/Be, and ^{11}B/^{10}B–at very low metallicity, where the primary and secondary origins differ most in their predictions.

It is just as important to firmly establish the nature and evolution of O/Fe; other metallicity indices, such as Mg, could help to clarify this question. These should be analyzed systematically as we have tried to do with oxygen. Gamma-ray line astronomy should also help to confirm the possibility of acceleration of freshly synthesized nuclei in superbubbles and OB associations. This will be a key objective for the European INTEGRAL mission. Thus, we are pleased to report that the nature of LiBeB evolution, is a problem that is ripe for new and precision observations, which can go far to reveal the origin and history of accelerated particles in the Galaxy.

We thank Andrei Bykov for graciously making available data files for his published spectra. We thank Roger Cayrel and Evan Skillman for fruitful discussions. This work was supported in part by DoE grant DE-FG02-94ER-40823 at the University of Minnesota.

REFERENCES

Alonso, A., Arribas, S., & Martinez-Roger, C. 1996a, A & AS, 117, 227

———. 1996b, A & A, 313, 873

Axer, M., Fuhrmann, K., & Gehren, T. 1994, A & A, 291, 895

Bessell, M.S., Hughes, S.M.G., & Cotrell, P.L. 1984, Publ Ast Soc Aust, 5, 547

Boesgaard A. & King J.R. 1993, AJ, 106, 2309

Boesgaard, A.M., King, J.R., Deliyannis, C.P., & Vogt, S.S. 1999, AJ, 117, 492

Boesgaard, A.M., Deliyannis, C.P., King, J.R., Ryan, S.G., Vogt, S.S., & Beers, T.C. 1999, AJ, 117, 1549

Bonifacio, P. & Molaro, P. 1997, MNRAS, 285, 847

Bykov, A.M. 1995, Space Sci. Rev, 74, 397

Bykov, A.M. 1999, in "LiBeB, cosmic rays and related X-and Gamma- Rays", eds. Ramaty *et al.* , ASP, vol. 171, p. 146

Carney, B.W. 1983, AJ, 83, 623

Cassé, M., & Goret, Ph. 1978, ApJ, 221, 703

Cassé, M., Lehoucq, R., & Vangioni-Flam, E. 1995, Nature, 373, 38

Delbourgo-Salvador, P., & Vangioni-Flam, E. 1993, in "Origin and Evolution of the elements", eds. N. Prantzos *et al.* , Cambridge U. press, p. 132.

Duncan, D., Primas, F., Rebull, L.M., Boesgaard, A.M., Deliyannis, C.P., Hobbs, L.M., King., & Ryan, S.G. 1997, ApJ 488, 338

Ellison, D.C., Drury, L.O'C., & Meyer, J.P. 1997, ApJ, 487, 197

Fields, B.D., & Olive, K.A. 1999, ApJ, 516, 797

———. 1999, New Astron., 4, 255

Fields, B.D., Olive, K.A., & Schramm, D.N. 1994, ApJ, 435, 185

———. 1995, ApJ, 438, 854

Fuhrmann, K. 1998, A&A, 338, 161

Fuhrmann, K., Axer, M., & Gehren, T. 1993, A&A, 271, 451

Fuhrmann, K., Pfeiffer, M., Frank, C., Reetz, J., & Gehren, T. 1997, A&A, 323, 900

Fulbright, J.P., & Kraft, R.P. 1999, AJ

García-López, R.J., *et al.* , Ap.J. 500 (1998) 241

Gilmore, G., Gustafsson, B., Edvardsson, B. & Nissen, P.E. 1992, Nature 357, 379

Higdon, B., Lingenfelter, R.E., & Ramaty, R. 1998, ApJ, 509, L33

Hobbs, L.M. & Thorburn, J.A. 1996, AJ, 111, 2106

Israelian, G., García-López, R.J., & Rebolo, R. 1998, ApJ, 507, 805

King, J.R. 1993, AJ, 106,1206

Kiselman, D. 1994, A&A, 286, 169

Kiselman, D. & Carlsson, M. 1996, A&A, 311, 680

Lemoine, M., Vangioni-Flam, E., & Cassé, M. 1998, ApJ, 499,735

MacLow, M.M., McCray, R. 1988, ApJ, 324, 776

Meneguzzi, M. , Audouze, J., & Reeves, H. 1971, A&A, 15, 337

Meyer, J.P., Drury, L.O'C., & Ellison, D.C. 1997, ApJ, 487, 182

Molaro, P., Bonifacio, P., Castelli, F., & Pasquini, L. 1997, A&A, 319, 593

Molaro, P., Primas, F., & Bonifacio, P. 1995, A & A, 295, L47

Mori, M. 1997, ApJ, 478, 225

Nissen, P.E., Gustafsson, B., Edvardsson, B., & Gilmore, G. 1994, A & A, 285, 440

Olive, K.A., Prantzos, N., Scully, S., & Vangioni-Flam, E. 1994, ApJ, 424, 666

Parizot, E. 1998, A&A 331, 726

Prantzos, N., Cassé, M., & Vangioni-Flam, E. 1993, ApJ, 403, 630

Primas, F. 1995, Ph.D. thesis

Primas, F., Duncan, D.K., Peterson, R.C., & Thorburn, J.A. 1999, A&A, 343, 545

Ramaty, R., Kozlovsky, B., Lingenfelter, R.E., & Reeves, H. 1997, ApJ, 488, 730

Ramaty, R., & Lingenfelter, R.E. 1999, in "LiBeB Cosmic Rays and Related X- and Gamma-Rays, eds. Ramaty *et al.* , ASP, Vol. 171, p. 104

Ramaty, R., Scully, S., Lingenfelter, R. and Kozlovsky, B. 1999 (astro-ph/9909021)

Read, S. & Viola, V. 1984, Atomic Data Nucl. Data Tab., 31, 359

Rebolo, R., Molaro, P., Abia, C., Beckman J.E. 1988, A&A, 193, 193

Rebolo R. *et al.* 1993, in *Origin and Evolution of the Elements* eds. N. Prantzos, E. Vangioni-Flam & M. Cassé (Cambridge University Press), p. 149

Reeves, H., Fowler, W.A., & Hoyle, F. 1970, Nature, 226, 727

Ryan, S.G., Beers, T.C., Olive, K.A., Fields, B.D., & Norris, J.E. 1999, Nature, submitted (astro-ph/9905211)

Ryan, S., Bessell, M., Sutherland, R.& Norris, J. 1990, ApJ, 348, L57

Ryan, S.G., Norris, J.E., Bessell, M.S., & Deliyannis, C. 1992, ApJ, 388, 184

Shigeyama, T. & Tsujimoto, T. 1998, ApJ, 507, L135

Spitzer, L. 1990, ARAA, 28, 71

Strong, A. W., & Moskalenko, I. V. 1998, ApJ, 509, 212

Strong, A.W., & Moskalenko, I.V. 1999, in LiBeB Cosmic Rays and Gamma-Ray Line Astronomy, ASP Conference Series v. 171, eds. R. Ramaty, E. Vangioni-Flam, M. Cassé, & K. Olive, 162

Tenorio-Table, G., & Bodenheimer, P. 1988, ARAA, 36, 145

Thévenin, F., & Idiart, T.P. 1999, ApJ, 521,753

Thielemann, F.K., Nomoto, K., & Hashimoto, M. 1996, ApJ, 460, 108

Thomas, D., Schramm, D.N., Olive, K.A., & Fields, B.D. 1993, ApJ, 406, 569

van den Hoek, L.B., & Groenewegen, M.A.T. 1997, A&AS, 123, 305

Vangioni-Flam E., & Cassé, M. 2000, Natal IAU Conference

Vangioni-Flam, E., Cassé, M., & Audouze, J. 1999, Phys. Rept., in press

Vangioni-Flam, E., Cassé, M., Audouze, J., & Oberto, Y. 1990, ApJ, 364, 568

Vangioni-Flam, E., Cassé, M., Cayrel, R., Audouze, J., Spite, M., & Spite, F. 1999, New Astr., in press (astro-ph/9811327)

Vangioni-Flam, E., Cassé, M., Fields, B.D., & Olive, K.A. 1996, ApJ, 468, 199

Vangioni-Flam, E., Ramaty, R., Olive, K.A., & Cassé, M. 1998, AA 337, 714

Walker, F., Kerp, J., Duric, N. Brinds, E., & Klein, U. 1998, ApJ, 502, L143

Woosley, S.E. Hartmann, D.H., Hoffman, R.D., & Haxton, W.C., 1990, ApJ, 356, 272

Woosley, S.E., & Weaver, T.A. 1995, ApJS 101, 181

This preprint was prepared with the AAS LaTeX macros v4.0.

Figure Captions

1. Source and propagated spectra for accelerated particles.
   Top Panel: Source spectra $Q(E)$ for the GCR (solid curve) and SAP (dashed curve) components. E is the kinetic energy per nucleon in MeV/n, while the units of $Q(E)$ are arbitrary, and the relative scaling of the two components has been adjusted for clarity.
   Bottom Panel: Propagated spectra corresponding to the sources in the top panel.

2. Oxygen (solid line) and iron (dashed line) yield estimates, calculated from the numerical model. For derivation see discussion in text.
   Top Panel: Yields versus time.
   Bottom Panel: Results from top panel translated to a mass scale via the stellar mass-lifetime relation $\tau(m)$.

3. Be *vs* O (*top panel*) and B *vs* O (*bottom panel*). Data shown are the Balmer points, which are found (Table 5) to have a break point as indicated. Models are adjusted to have the break point and O/Fe slope of these data.

4. As in Fig. 3, for the IRFM1 data and corresponding model.

5. As in Fig. 3, for the IRFM2 data and corresponding model.

6. The B/Be ratio *vs* O. Shown are the Balmer data and the corresponding model.

7. As in Fig. 6, for the IRFM1 data and corresponding models.

8. As in Fig. 6, for the IRFM2 data and corresponding models.

9. Be and B vs Fe, for the Balmer data and break point. As discussed in the text, Fe in the model is obtained by scaling from O, using the observed relation $[\mathrm{O/H}] = \omega_{\mathrm{O/Fe}}[\mathrm{Fe/H}]$, with $\omega_{\mathrm{O/Fe}}$ from Table 1.

10. As in Fig. 9, for the IRFM1 data and corresponding models.

11. As in Fig. 9, for the IRFM2 data and corresponding models.

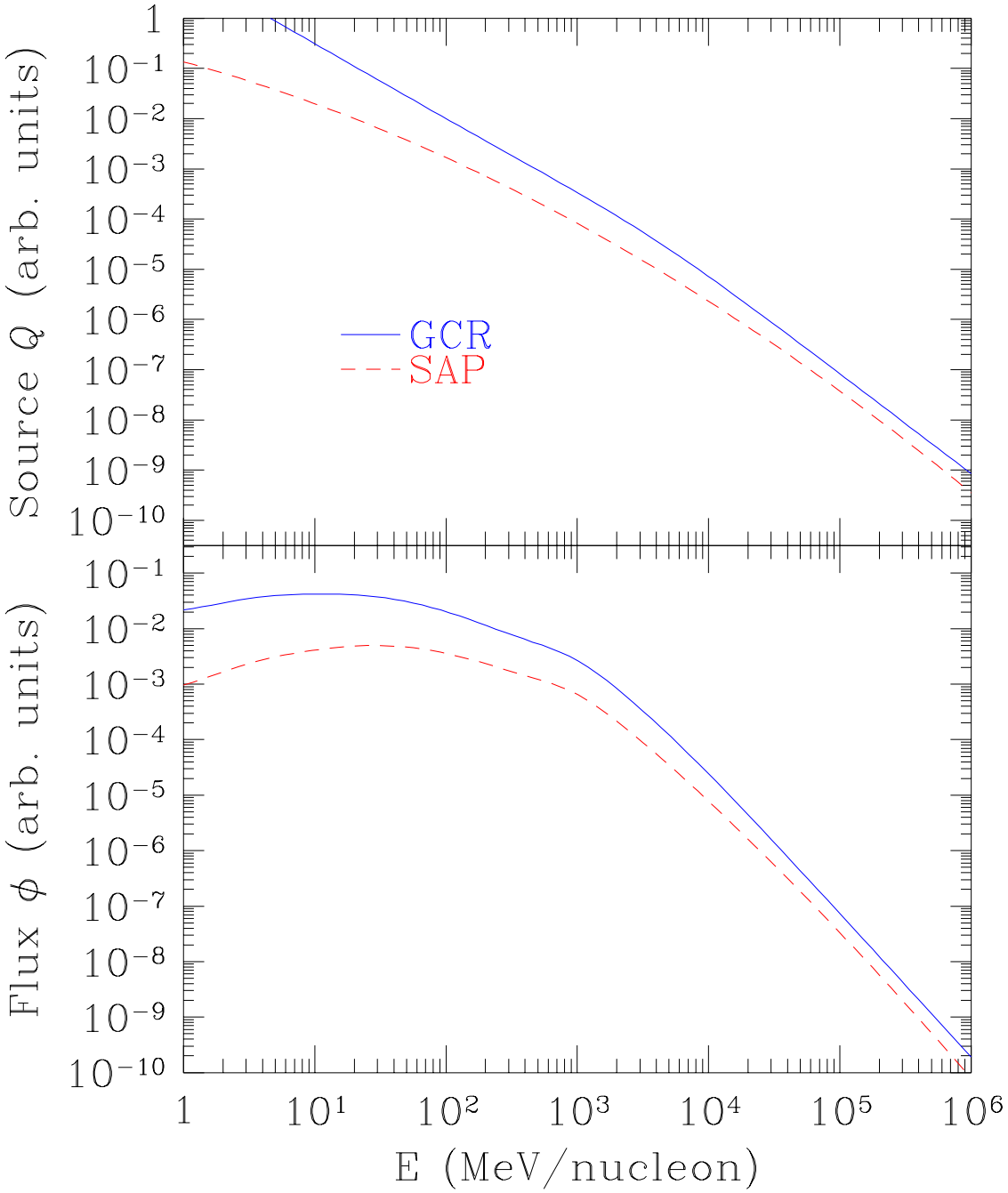
Source Q (arb. units)
Flux ϕ (arb. units)
GCR
SAP
E (MeV/nucleon)
1
10^{-1}
10^{-2}
10^{-3}
10^{-4}
10^{-5}
10^{-6}
10^{-7}
10^{-8}
10^{-9}
10^{-10}
10^{1}
10^{2}
10^{3}
10^{4}
10^{5}
10^{6}

Fig. 1.—

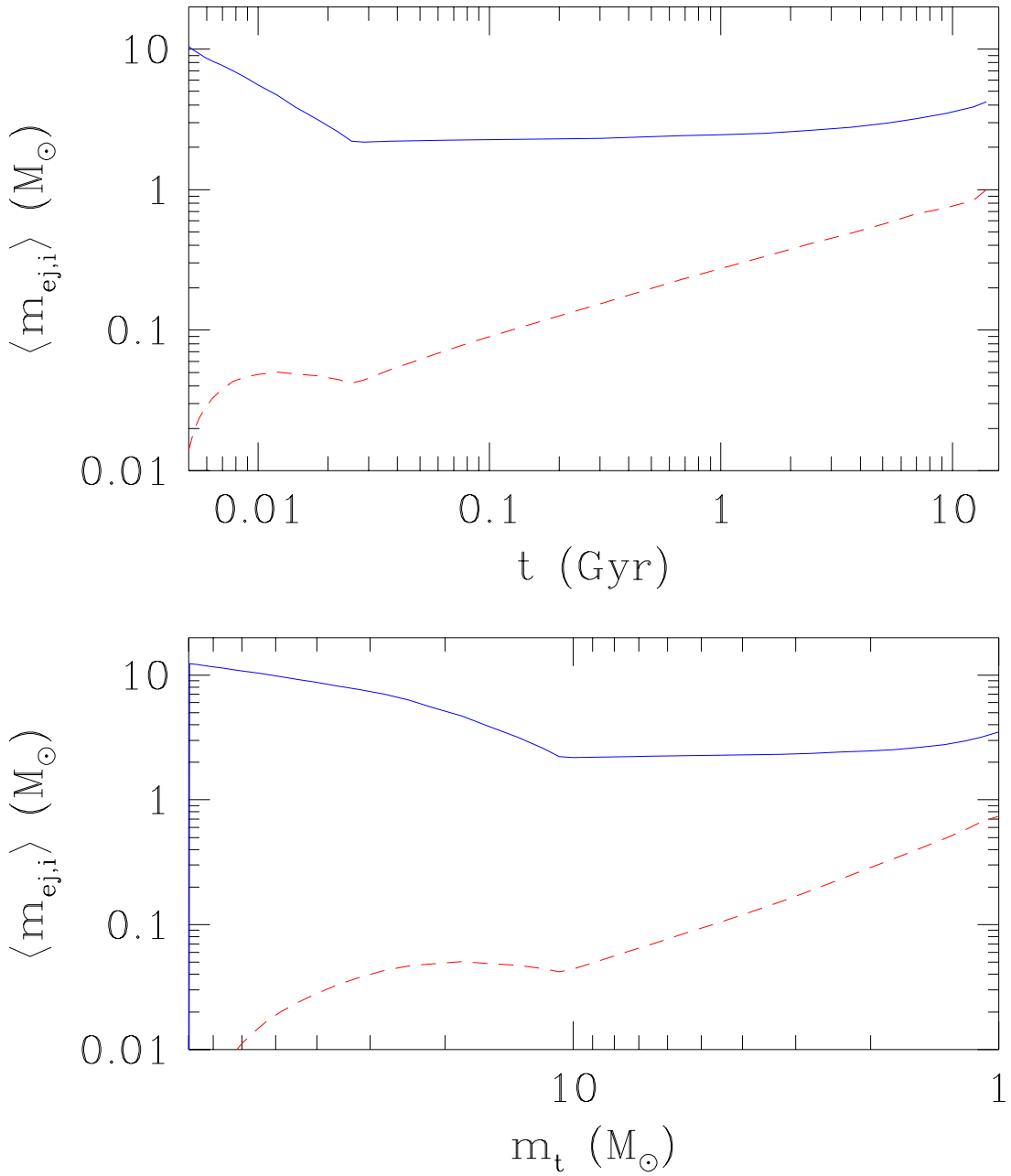
10
1
0.1
0.01
$\langle m_{ej,i} \rangle$ ($M_\odot$)
0.01
0.1
1
10
t (Gyr)
10
1
0.1
0.01
$\langle m_{ej,i} \rangle$ ($M_\odot$)
10
1
m_t ($M_\odot$)

Fig. 2.—

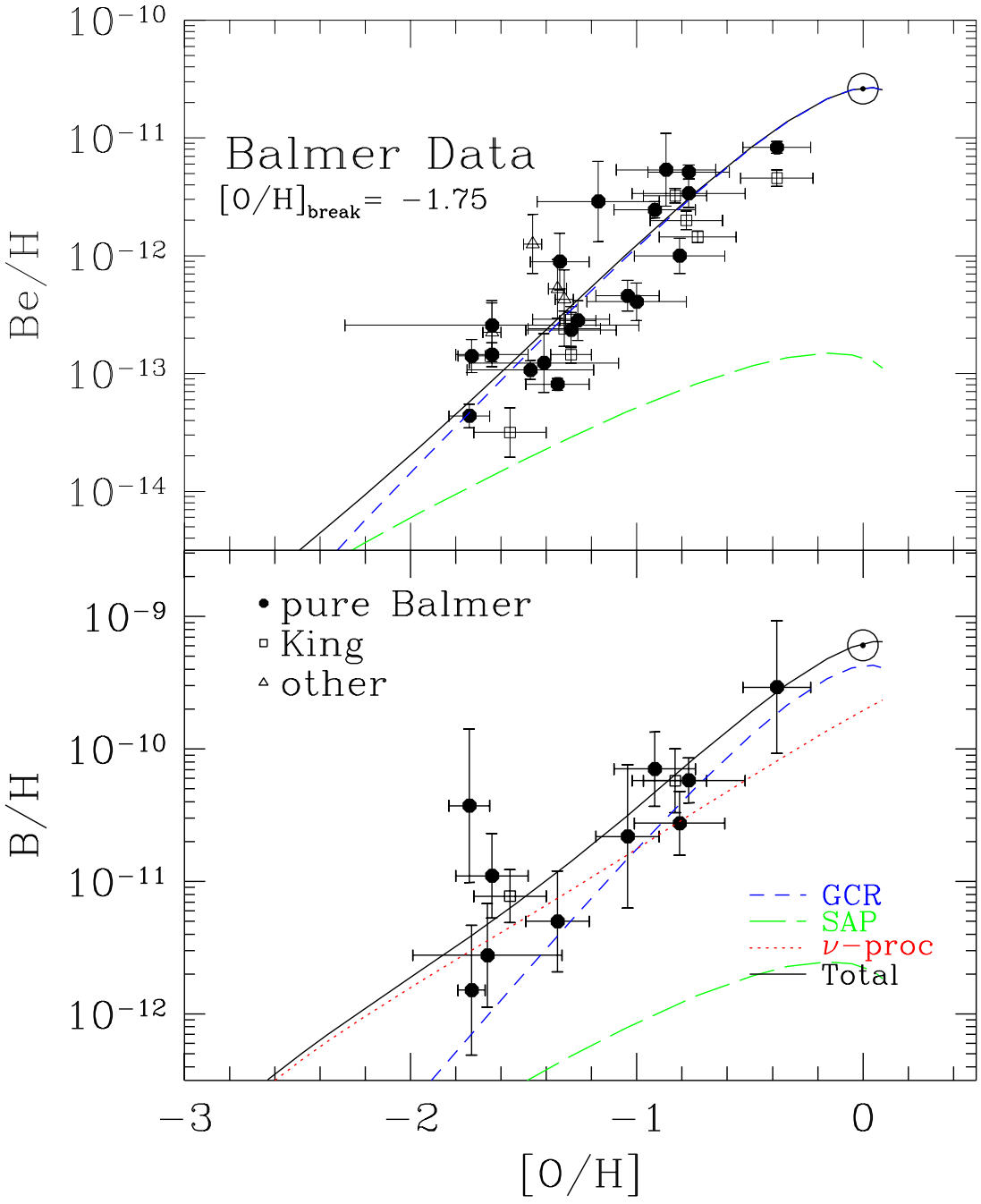
Balmer Data
[O/H]break= −1.75
Be/H
B/H
• pure Balmer
▫ King
▵ other
GCR
SAP
ν−proc
Total
[O/H]

Fig. 3.—

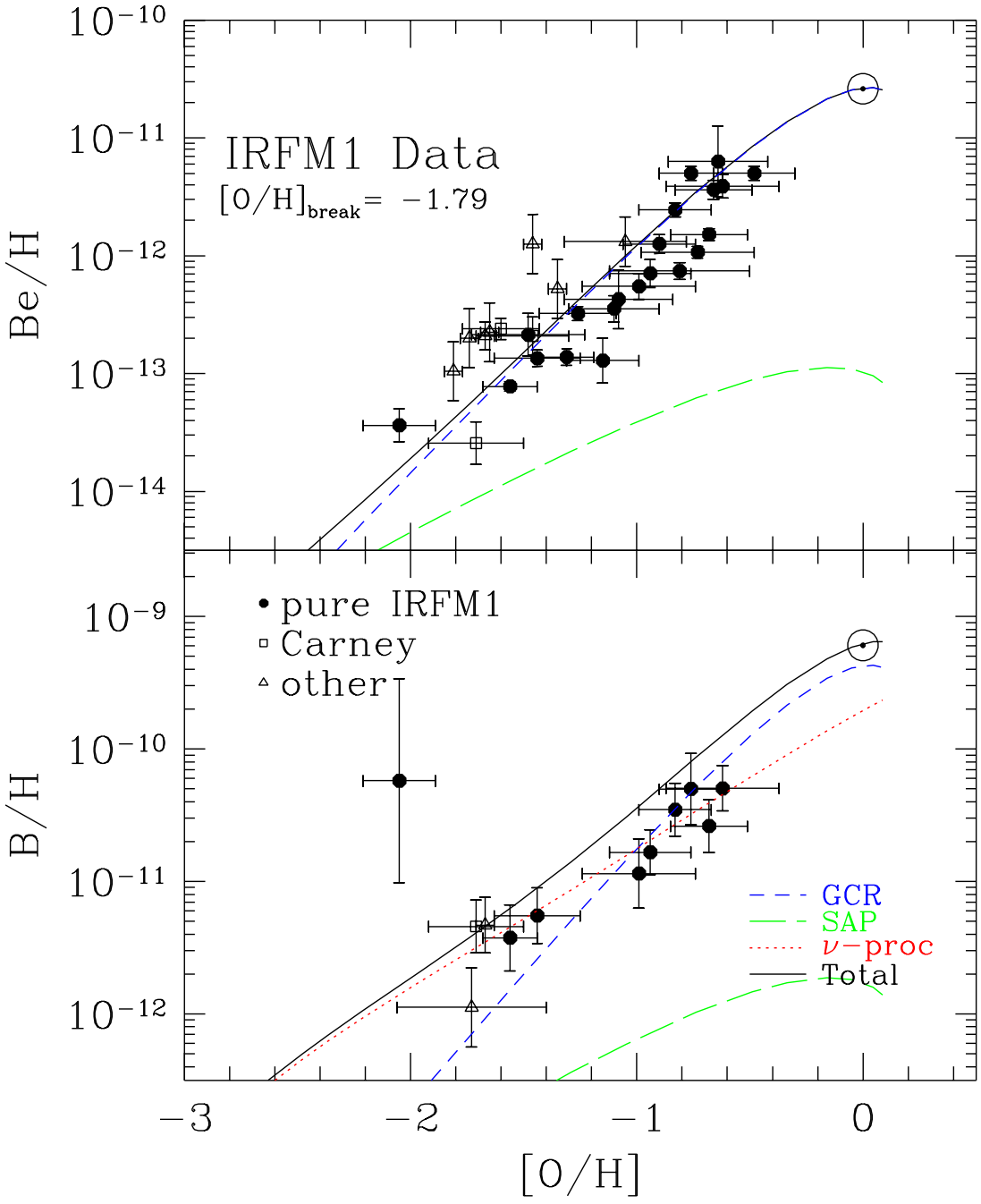
IRFM1 Data
[O/H]break= −1.79
Be/H
B/H
• pure IRFM1
▫ Carney
▵ other
GCR
SAP
ν−proc
Total
[O/H]

Fig. 4.—

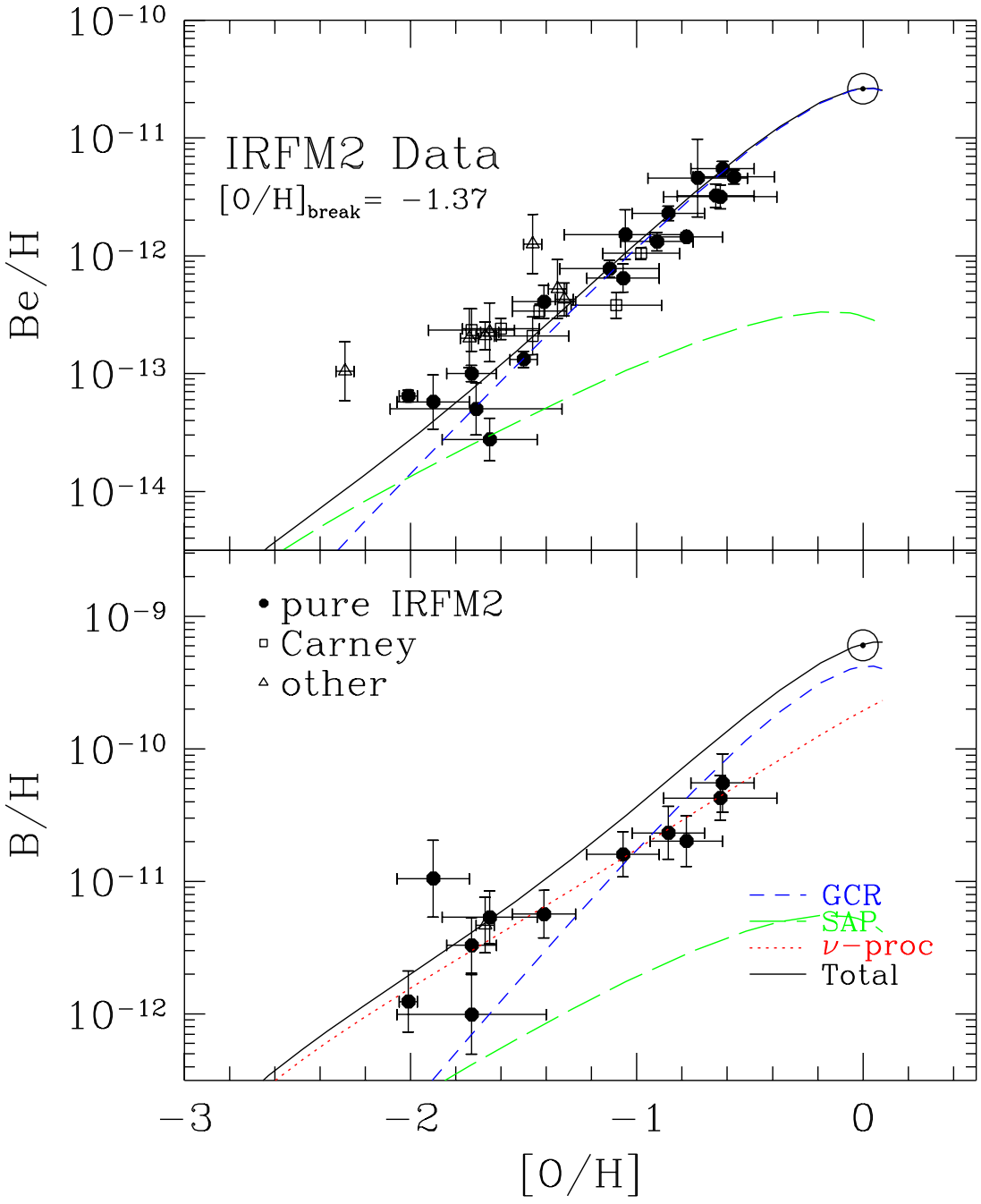
IRFM2 Data
[O/H]break= −1.37
Be/H
B/H
• pure IRFM2
▫ Carney
▵ other
GCR
SAP
ν−proc
Total
[O/H]

Fig. 5.—

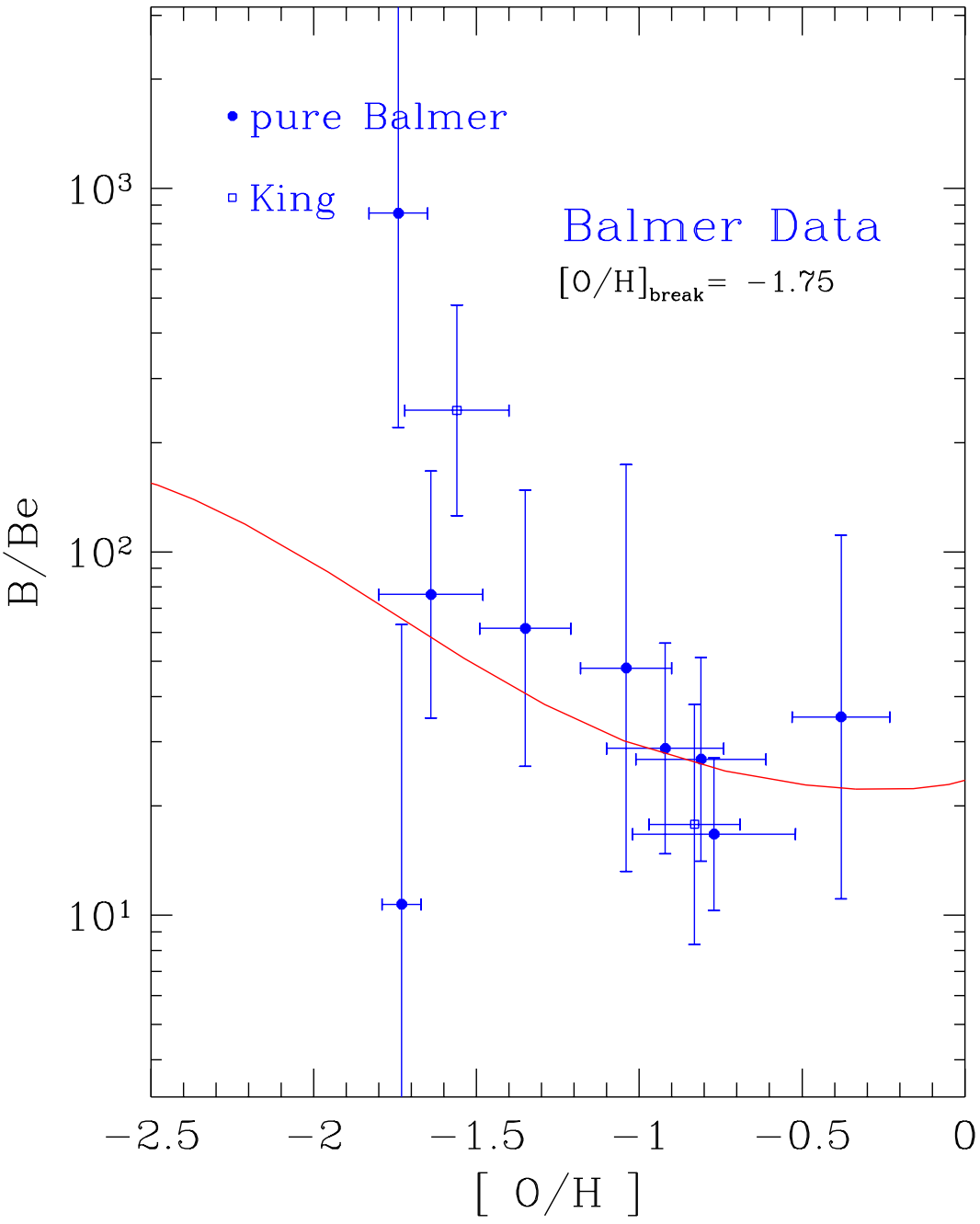
• pure Balmer
King
Balmer Data
[O/H]break= −1.75
B/Be
10³
10²
10¹
−2.5
−2
−1.5
−1
−0.5
0
[O/H]

Fig. 6.—

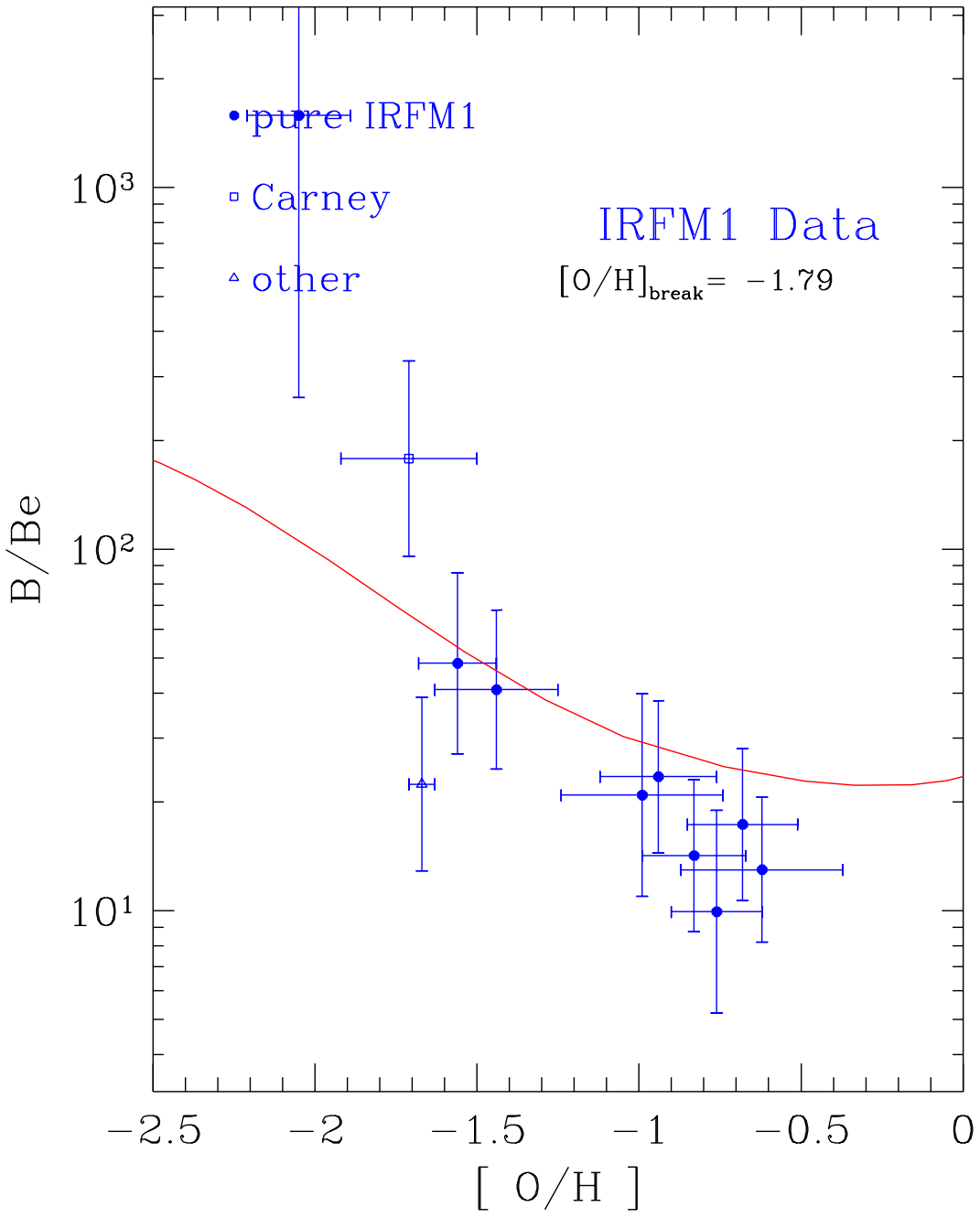
pure IRFM1
Carney
other
IRFM1 Data
[O/H]break= −1.79
B/Be
10³
10²
10¹
−2.5
−2
−1.5
−1
−0.5
0
[O/H]

Fig. 7.—

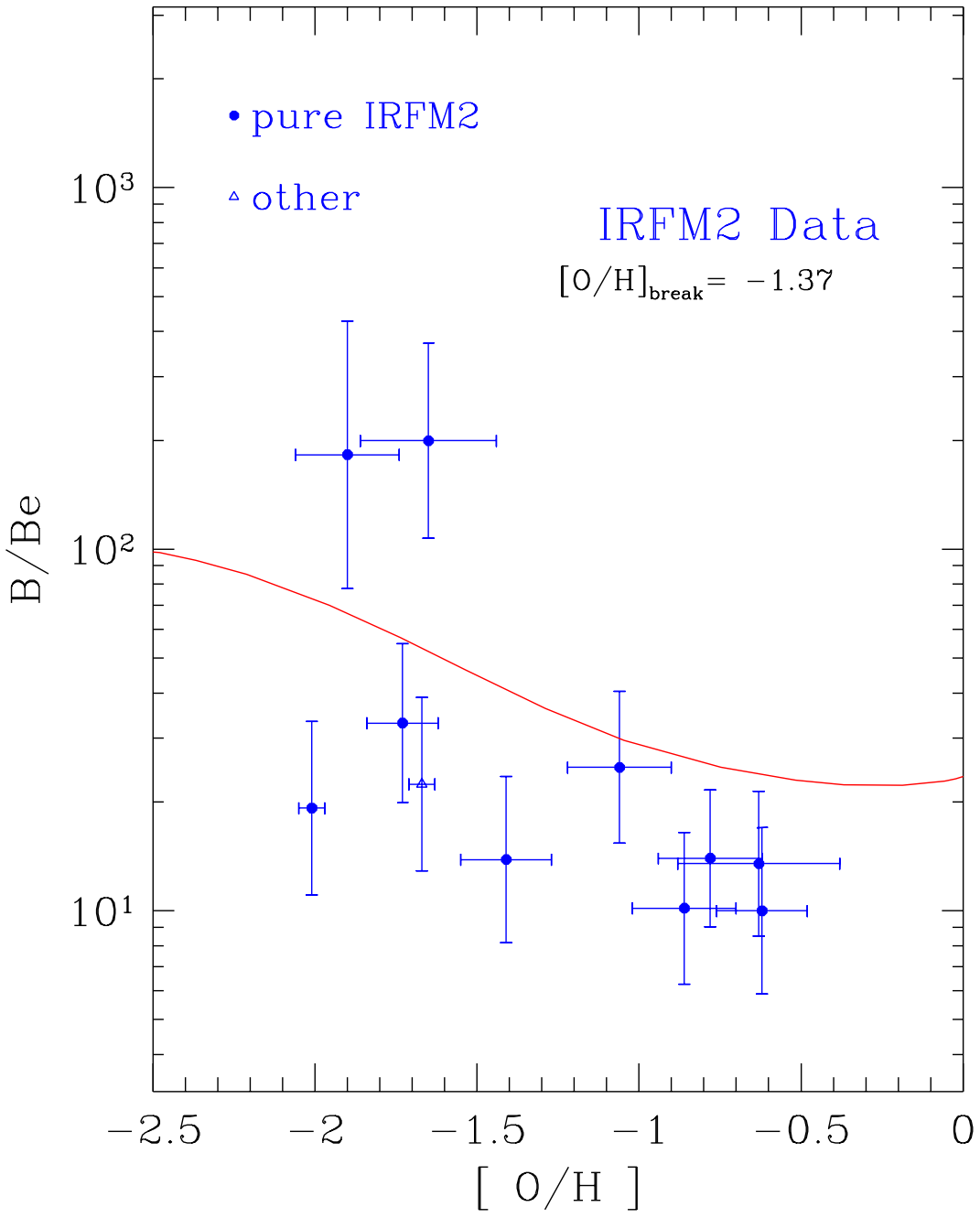
• pure IRFM2
▵ other
IRFM2 Data
[O/H]break= −1.37
B/Be
10³
10²
10¹
−2.5
−2
−1.5
−1
−0.5
0
[O/H]

Fig. 8.—

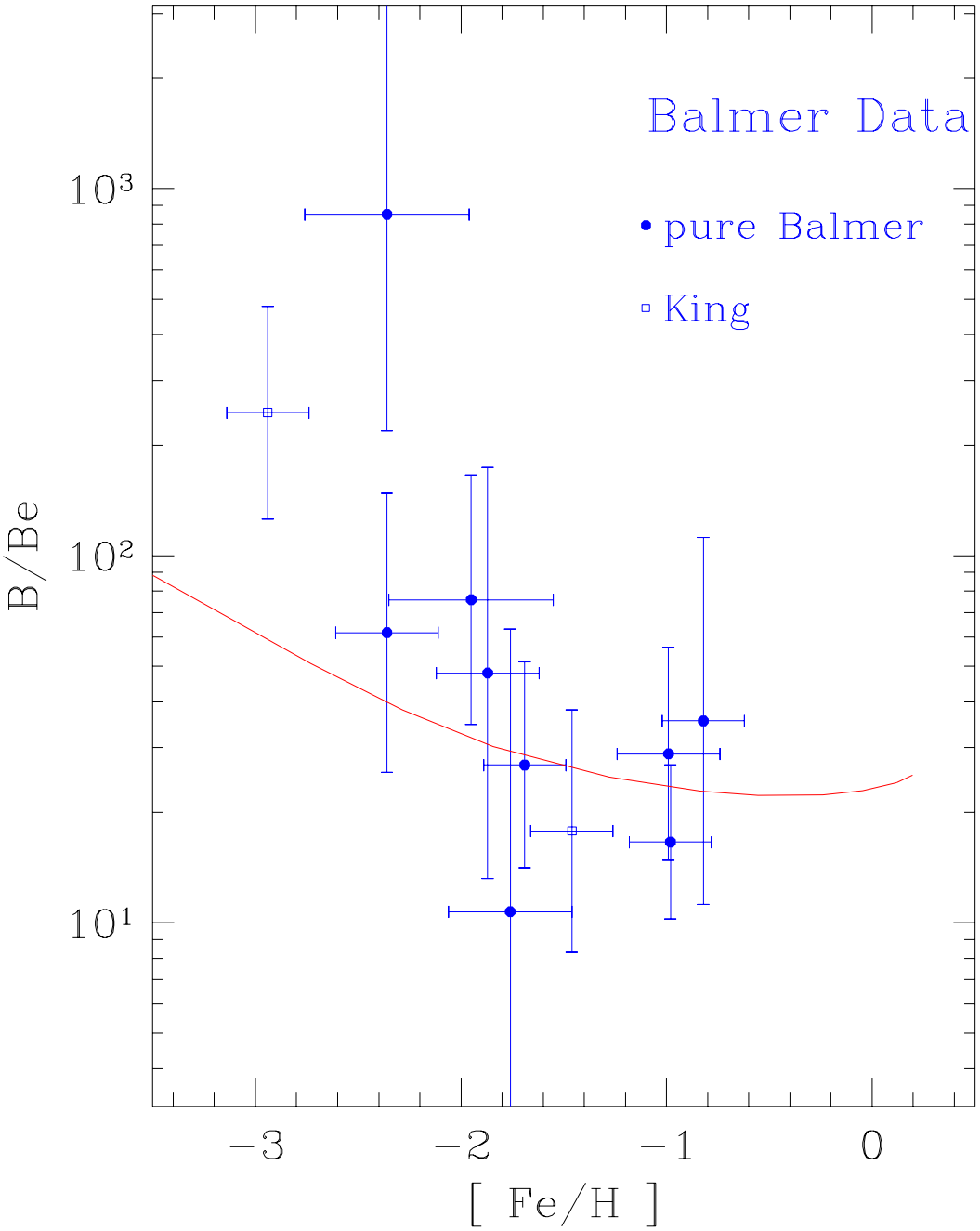

Fig. 9.—

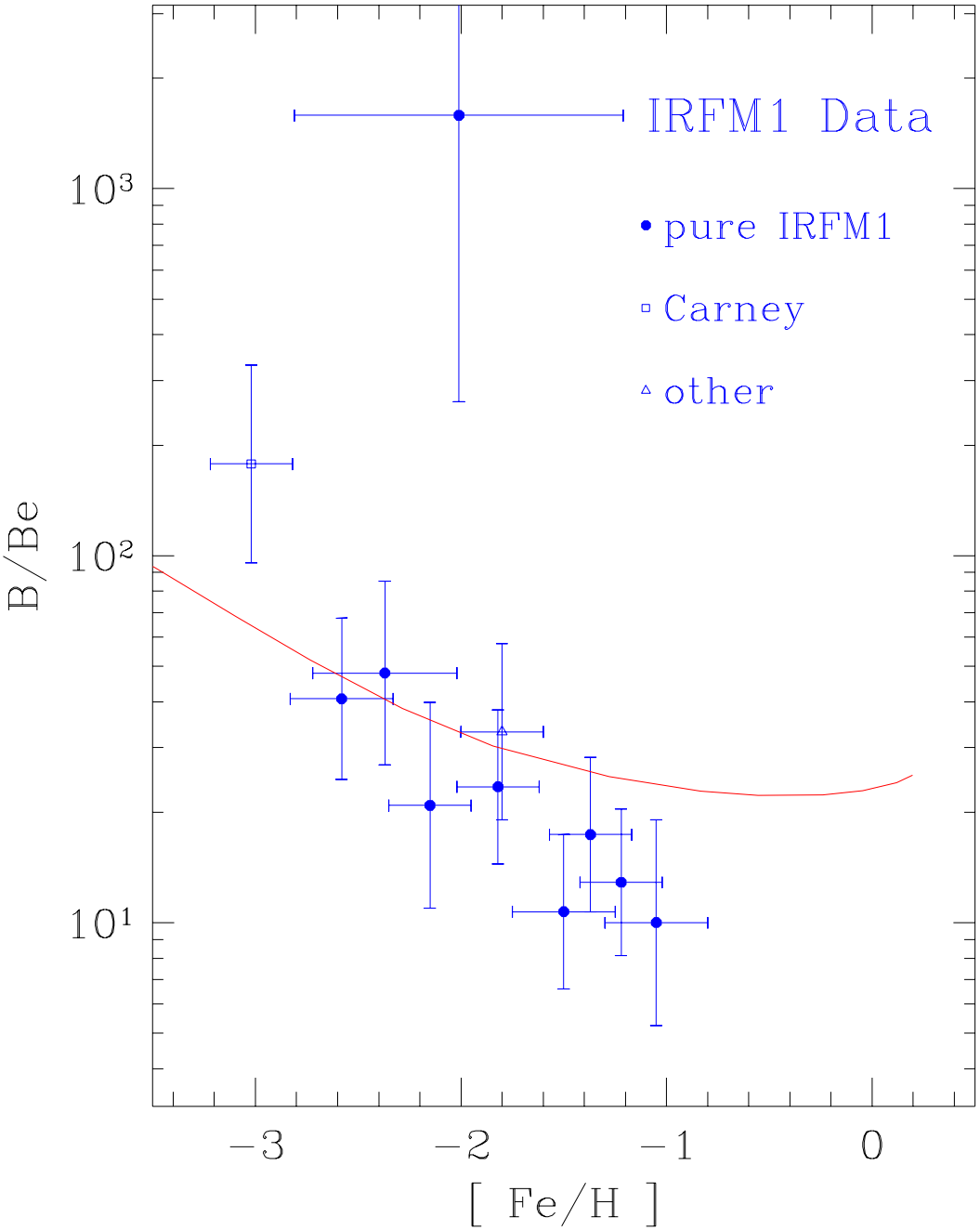

Fig. 10.—

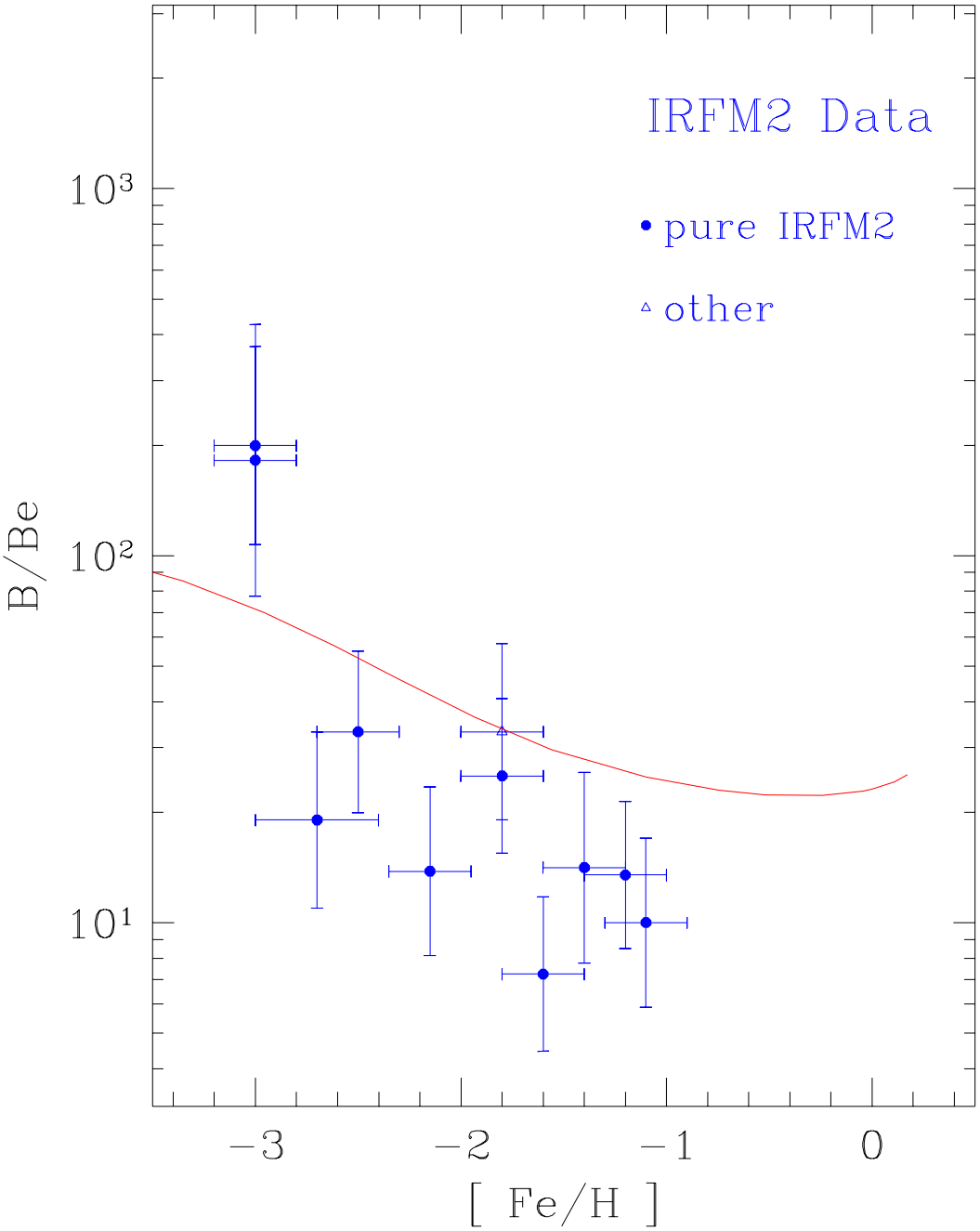

Fig. 11.—